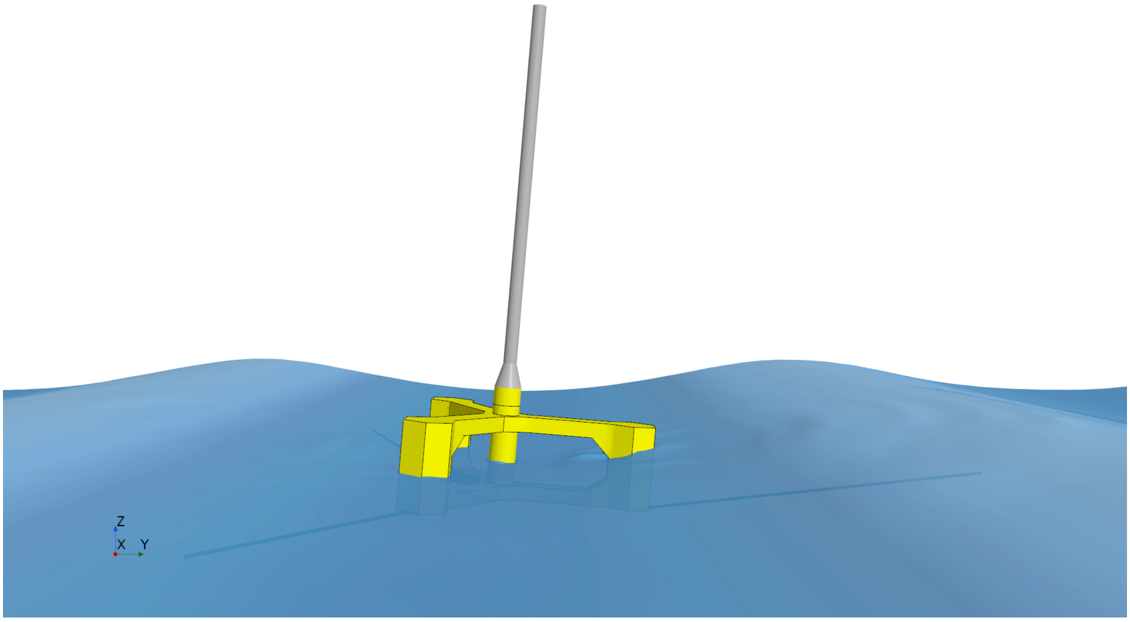

CFD Simulation of a Semi-Submersible Floating Wind Platform in Waves

Balancing Accuracy and Efficiency in Simulation of Wave-Structure Interaction

Master’s thesis in Sustainable Energy Systems

JOHANNA LARNERT

DEPARTMENT OF MECHANICS AND MARITIME SCIENCES

CHALMERS UNIVERSITY OF TECHNOLOGY
Gothenburg, Sweden 2025
www.chalmers.se

Master's thesis 2025

CFD Simulation of a Semi-Submersible Floating Wind Platform in Waves

Balancing Accuracy and Efficiency in Simulation of Wave-Structure Interaction

JOHANNA LARNERT

Department of Mechanics and Maritime Sciences
Marine Technology Division
Chalmers University of Technology
Gothenburg, Sweden 2025

CFD Simulation of a Semi-Submersible Floating Wind Platform in Waves
Balancing Accuracy and Efficiency in Simulation of Wave-Structure Interaction
JOHANNA LARNERT

Supervisor: Joakim Hägglund, Aker Solutions
Examiner: Hua-Dong Yao, Department of Mechanics and Maritime Sciences

Master's Thesis 2025
Department of Mechanics and Maritime Sciences
Marine Technology Division
Chalmers University of Technology
SE-412 96 Gothenburg
Telephone +46 31 772 1000

Cover: Visualization of the developed CFD model of the YFloat.

Typeset in LaTeX
Gothenburg, Sweden 2025

CFD Simulation of a Semi-Submersible Floating Wind Platform in Waves
Balancing Accuracy and Efficiency in Simulation of Wave-Structure Interaction
JOHANNA LARNERT
Department of Mechanics and Maritime Sciences
Chalmers University of Technology

Abstract

Offshore wind power is a promising solution for large-scale renewable energy production, offering benefits such as abundant offshore space and higher energy output. One type of floating platform is semi-submersibles, which combine buoyancy stabilization with catenary mooring systems. This thesis presents the development of a numerical model of the YFloat semi-submersible floating offshore wind platform using the CFD software StarCCM+, intending to achieve a balance between computational efficiency and solution accuracy.

To support model development, initial wave simulations were conducted without the floater to investigate mesh requirements for accurately capturing wave-induced currents and wave heights. The results indicated that capturing the wave-induced current required a fine mesh with at least 25 cells per wave height and 132 cells per wavelength, while wave heights could be represented adequately with a significantly coarser mesh.

Consecutive full-scale simulations included the floater and were validated against experimental model test data. A free decay simulation was used to confirm the floater's dynamic properties, showing less than 5 % deviation in rotation around the x-axis compared to test results. Simulations in regular waves focused on the spatial and temporal resolution influence on motion responses and wave height. The best compromise between accuracy and efficiency was achieved with 10 cells per wave height and a time step of $\Delta t = 0.02$ s. This configuration required 2.8 hours of simulation time, saving 7.3 hours compared to the finest spatial resolution, which took 10.1 hours (a 72.3% reduction), and 9.7 hours compared to the finest temporal resolution, which took 12.5 hours (a 77.6% reduction). The numerical results showed strong agreement with experimental data, validating the CFD model.

Keywords: Computational fluid dynamics, floating offshore wind, semi-submersible.

Acknowledgements

First of all, I would like to thank my amazing supervisor Joakim Hägglund at Aker Solutions for his invaluable support and guidance through this work! Moreover, I would like to thank Peder Hesten at Aker Solutions for his continuous guidance and input regarding hydrodynamics and model testing. A special thank you to Kristian Målbakken for always cheering me on and providing me with candy during tough times. Thank you to my parents for always being my biggest supporters and best friends! A big thank you to Professor Hua-Dong Yao for being my examiner and for always taking the time to answer my questions, no matter how big or small. Lastly, thank you to all my wonderful and supportive friends who have made my time at Chalmers so special!

Johanna Larnert, Gothenburg, May 2025

List of Acronyms

Below is the list of acronyms that have been used throughout this thesis listed in alphabetical order:

BEM	Boundary Element Method
BEMT	Blade Element Method Theory
CFD	Computational Fluid Dynamics
DFBI	Dynamic Fluid Body Interaction
DNS	Direct Numerical Simulations
DOF	Degrees of Freedom
FOWT	Floating Offshore Wind Turbine
ME	Morison Equation
RANS	Reynolds-Averaged Navier-Stokes
SST	Shear Stress Transport
TLP	Tension Leg Platform
VOF	Volume of Fluid

Nomenclature

Below is the nomenclature of indices, sets, parameters, and variables that have been used throughout this thesis.

Indices

i, j	Indices for spatial dimensions
t	Time index

Parameters

Δt	Time discretization (time step)
g	Acceleration due to gravity
L_M	Characteristic length of the model
L_F	Characteristic length of the full scale
F_r	Froude number

Variables

ρ	Density
v	Velocity magnitude or vector
v_i	Velocity component in direction i
x_i	Coordinate in direction i
p	Pressure
ν	Kinematic viscosity
υ	Fluid kinematic viscosity (alternative symbol)
k	Turbulent kinetic energy
ε	Turbulent dissipation rate

ω	Specific dissipation rate
α	Indicator function (volume fraction)
τ_{ij}	Viscous stress tensor
$\langle v_i \rangle$	Mean velocity component
v'_i	Fluctuating velocity component
$\langle v'_i v'_j \rangle$	Reynolds stress component
η	Free surface elevation
u_*	Friction velocity
y^+	Dimensionless wall distance
δ	Boundary layer thickness

Contents

List of Figures

List of Tables

1

Introduction

1.1 Floating Offshore Wind Power

The transition from a fossil fuel-dependent energy system to a renewable energy system is one of today's society's biggest challenges. The decade between 2014 and 2023 was the warmest decade ever recorded, according to the International Renewable Energy Agency's World Energy Transition Outlook 2024 report [1]. Despite the various ambitious commitments made to reduce carbon emissions, such as the ones made during COP28 in 2023, the energy transition still has a long way to go [10]. While the renewable deployment in the power sector is growing at a record rate, fossil fuels continue to dominate the energy mix of major economies. In 2023, a record-high 37.4 Gt of global-energy-related carbon dioxide emissions were released into the atmosphere. Hence, further acceleration of the energy transition is of utter importance.

Offshore wind power is seen as one of the most promising alternatives for large-scale renewable energy production [22]. The attractiveness of offshore wind is mainly related to the vast availability of offshore locations, high energy output, and its scalability opportunities. Fixed-bottom offshore wind turbines currently dominate the market, but floating offshore wind technology is rapidly gaining interest. Floating Offshore Wind Turbines (FOWTs) allow for offshore wind applications at greater water depths, giving access to significantly more wind resources. In 2023, the installed capacity of floating offshore wind power was estimated to be 270 MW [10]. With an ambitious global pipeline of approximately 244 GW in upcoming projects, the industry is on a strong trajectory for significant growth.

1.2 Floating platform design

When designing the floating platforms on which the wind turbines are installed, it is of great importance to find a balance between ensuring sufficient stability for effective turbine control and operation, and allowing enough flexibility for the platform to respond to environmental forces such as wind and waves [3]. Due to the absence of rigid foundations, such platforms have six Degrees of Freedom (DOFs). These consist of three translational and three rotational DOFs, as described in Figure 1.1.

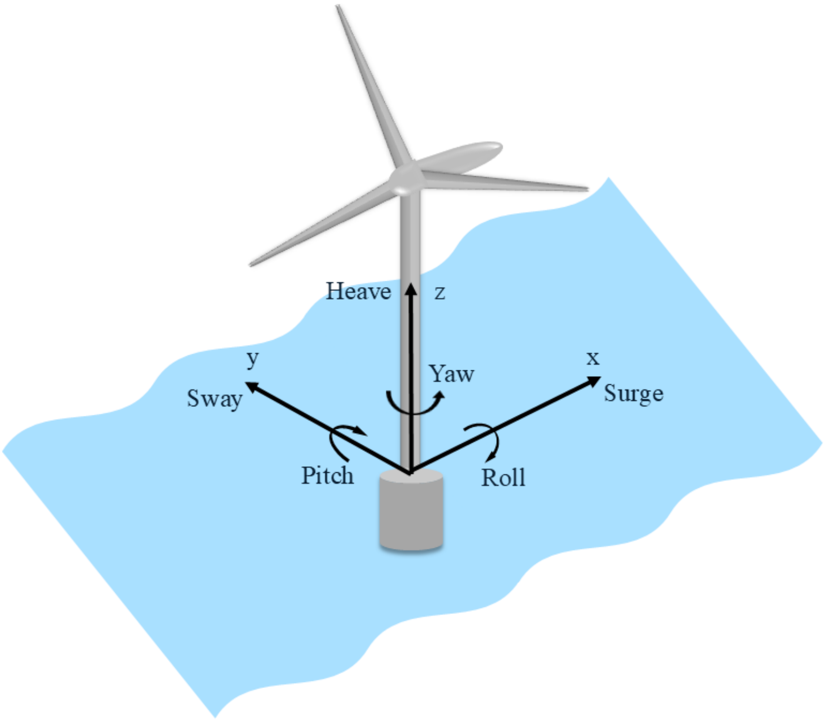

Figure 1.1: Floating offshore wind turbine platform with six DOFs.

There are four main types of FOWTs platforms: semi-submersibles, barges, tension-leg platforms (TLPs), and spar buoys [8]. Semi-submersible floating platforms combine buoyancy stabilization with a catenary mooring system for stability. Furthermore, semi-submersibles have a shallow draft which allows for deployment in depths of about 40-50 meters and enables installation of the system in a harbor, which then can be transported offshore by tug boats. The main advantage of this kind of platform is its adaptability to various depths, enabled by the adjustable ballast system. In Figure 1.2, the semi-submersible FOWT YFloat$^{\text{TM}}$ developed by Aker Solutions is visualized.

Figure 1.2: The Semi-submersible FOWT YFloat^{TM} [19].

Numerical and physical modeling are important tools in developing the FOWT concepts. There are three approaches to analyzing the performance of a FOWT, with the most simple being the uncoupled approach [8]. This approach simplifies the analysis process by analyzing the hydrodynamics and aerodynamics separately. This can be done by for example subjecting the floater to wave conditions only in a wave-testing facility or through a numerical model. The partially coupled approach considers both aerodynamic and hydrodynamic factors, although one is usually simplified to better resolve the behavior of the other. For example, when the focus is on the aerodynamics, the hydrodynamics can be simulated using an induced oscillation technique. Lastly, the fully coupled approach captures the true behavior of FOWTs under simultaneous wave and wind loading, typically using detailed numerical simulations.

1.3 Numerical modeling of FOWT

A broad range of numerical techniques and software are used in the design of FOWTs [22]. Numerical models can be categorized as low, mid, and high fidelity, reflecting the level of computational resources and computational efficiency required. Low-fidelity models are typically used early on in the design process for parametric or sizing studies [16]. Mid-fidelity models, also called engineering tools, are commonly used for load analysis to examine operational and extreme conditions after the initial design has been developed. Lastly, high fidelity is mostly used for more detailed studies and can be used to tune lower fidelity tools.

Some commonly used mid-fidelity tools are OpenFAST, HAWC2, Bladed, SIMPACK, and OrcaFlex [16]. To simulate the aerodynamics, hydrodynamics and structural behavior of the FOWTs, these tools apply several different numerical methods, including Boundary Element Method (BEM), Morison Equation (ME), and Blade Element Momentum Theory (BEMT). Engineering tools have varying capabilities and are often coupled with frequency-domain solvers to obtain the hydrodynamic coefficients. Comparison of engineering tools with experimental data from a basin test of the DeepCwind semisubmersible has shown that all codes gave discrepancies in the results regarding the surge and pitch natural frequencies and motions, significantly impacting the accuracy of their prediction of the ultimate and fatigue loads of floating wind systems [17]. The reason behind this was found to be that the tools lack some of the physics required for accurate prediction of nonlinear, low-frequency loads. High fidelity modeling tools, such as computational fluid dynamics (CFD), should, with high accuracy, be able to predict the surge and pitch loads of a semi-submersible.

By creating trustworthy high-fidelity numerical tools, the aim is to reduce the need for costly and challenging model-scale experiments, overcoming significant financial and practical challenges [16].

1.4 Problem statement

This master's thesis aims to develop a numerical model of the semi-submersible floating platform concept YFloat$^{\text{TM}}$ in waves in the CFD software STAR-CCM+. Furthermore, the goal is to identify a simulation configuration that minimizes computational time while maintaining an acceptable level of accuracy. Existing basin model test data, including decay and regular wave conditions, will be used to verify the model. The following research questions will be addressed:

- What spatial resolution is required to accurately capture wave-induced currents and wave height when simulating a wave domain?
- What combination of spatial and temporal resolution provides the best balance between computational efficiency and accuracy when simulating the dynamic response of the floater in waves?

1.5 Limitations

For the scope of this study, the following limitations have been identified:

- No project-specific data related to environmental conditions is considered. Instead, generic wave data is used as the basis for the analysis.

- An uncoupled approach is employed, focusing exclusively on hydrodynamic effects. Consequently, the turbine and associated aerodynamic forces, including wind loads, are not considered.

2

Theory

2.1 Fundamentals of Fluid Mechanics

In fluid mechanics there are three fundamental laws that govern the conservation of mass, momentum and energy [11]. According to the conservation of mass, mass cannot be created or destroyed. For a control volume, the conservation of mass in a differential form is expressed in Equation 2.1.

$$\frac{\partial \rho}{\partial t} + \frac{\partial (\rho v_j)}{\partial x_j} = 0 \tag{2.1}$$

The conservation of momentum is described by Newton's second law which states that the rate of change of momentum of a body is equal to the forces applied. The conservation of mass for a Newtonian fluid is given by the Navier-Stokes equation as expressed in Equation 2.2 [2].

$$\frac{\partial v_i}{\partial t} + v_j \frac{\partial v_i}{\partial x_j} = -\frac{1}{\rho}\frac{\partial P}{\partial x_i} + \nu \frac{\partial}{\partial x_j}\left(\frac{\partial v_i}{\partial x_j} + \frac{\partial v_j}{\partial x_i}\right) + g_i \tag{2.2}$$

For incompressible fluids, Equation 2.1 and Equation 2.2 are abbreviated as described in Equation 2.3 and Equation 2.4.

$$\frac{\partial v_j}{\partial x_j} = 0 \tag{2.3}$$

$$\frac{\partial v_i}{\partial t} + v_j \frac{\partial v_i}{\partial x_j} = -\frac{1}{\rho}\frac{\partial P}{\partial x_i} + \nu \frac{\partial^2 v_i}{\partial x_j \partial x_j} \tag{2.4}$$

2.2 Turbulence

Turbulence is present in most fluid flows encountered in nature and engineering applications [11]. Despite this, it is very hard to predict the behavior of turbulent flows. The behavior of turbulent flows follows the Navier-Stokes equations, which are the foundation for CFD solvers. Turbulent flow structures span over a wide range of spatial and temporal scales, all interacting in a nonlinear, complex manner.

Hence, a very fine mesh is required to resolve the smallest scales, while still providing a computational domain sufficiently large to include the largest flow structures. Turbulent kinetic energy is transferred through the turbulent structures (eddies), from the largest scales to the smallest (Kolmogorov), where it is dissipated through viscous forces into heat.

Different numerical methods for turbulence are separated based on their spatial resolution. Numerically solving the Navier-Stokes equations without any modifications is called direct numerical simulations (DNS) [11]. Due to the high spatial and temporal grid resolution required, DNS is very costly. This, in combination with its limitations regarding Reynolds numbers, makes it unfeasible for most engineering applications. Large Eddy Simulations (LES) solve all turbulent scales except the Kolmogorov scales [14]. When using this method, a coarser grid may be used, which enables simulations of larger scales, but a sub-grid-scale turbulence model is required for the Kolmogorov scales.

2.2.1 Reynolds-Averaged Navier-Stokes

A third alternative for numerical simulations of turbulence is the Reynolds-Averaged Navier-Stokes (RANS) method [5]. In this method, the Navier-Stokes equations are Reynolds averaged, which significantly reduces the computational costs for solving the equations. To obtain the RANS equations, the flow variables, v_i, are decomposed into a mean value, $\langle v_i \rangle$, and the turbulent fluctuating part, v_i', as described in Equation 2.5.

$$v_i = \langle v_i \rangle + v_i' \tag{2.5}$$

There are three different Reynolds averaging methods from which the mean value can be obtained: time averaging, spatial averaging, and ensemble averaging. The average of the fluctuating part v_i' is zero for all three approaches, but $\langle v_i' v_i' \rangle \neq 0$, which also is true for $\langle v_i' v_j' \rangle$ in the case both turbulent velocities are correlated. By applying Reynolds averaging to the incompressible Navier-Stokes equations, Equation 2.6 and Equation 2.7 are obtained.

$$\frac{\partial \langle v_i \rangle}{\partial x_i} = 0, \tag{2.6}$$

$$\rho \frac{\partial \langle v_i \rangle}{\partial t} + \rho \langle v_j \rangle \frac{\partial \langle v_i \rangle}{\partial x_j} = \frac{\partial \langle p \rangle}{\partial x_i} + \frac{\partial (\tau_{ij} - \rho \langle v_i' v_j' \rangle)}{\partial x_j}, \tag{2.7}$$

The Reynolds stresses in the Reynolds averaged Navier-Stokes equation are easiest approximated using first-order closures, such as k-ε, k-ω and k-ω shear-stress transport (SST) [5]. These are two-equation models, meaning that in addition to the conservation equations, they also solve two transport equations which consider the historical effects such as convection and diffusion of turbulent energy.

2.2.2 The k - ε Turbulence Model

The basis of the k-ε model is the solution of the transport equations for the turbulent kinetic energy, k, and turbulent dissipation rate, ε [5]. These are presented in Equation 2.8 and Equation2.9.

$$\frac{\partial k}{\partial t} + \langle v_j \rangle \frac{\partial k}{\partial x_j} = \nu_t \left[\left(\frac{\partial \langle v_i \rangle}{\partial x_j} + \frac{\partial \langle v_j \rangle}{\partial x_i} \right) \frac{\partial \langle v_i \rangle}{\partial x_j} \right] - \varepsilon + \frac{\partial}{\partial x_j} \left[\left(\nu + \frac{\nu_t}{\sigma_k} \right) \frac{\partial k}{\partial x_j} \right] \tag{2.8}$$

$$\begin{aligned} \frac{\partial \varepsilon}{\partial t} + \langle v_j \rangle \frac{\partial \varepsilon}{\partial x_j} = C_{\varepsilon 1} \frac{\varepsilon}{k} \nu_t \left[\left(\frac{\partial \langle v_i \rangle}{\partial x_j} + \frac{\partial \langle v_j \rangle}{\partial x_i} \right) \frac{\partial \langle v_i \rangle}{\partial x_j} \right] \\ - C_{\varepsilon 2} \frac{\varepsilon^2}{k} + \frac{\partial}{\partial x_j} \left[\left(\nu + \frac{\nu_t}{\sigma_\varepsilon} \right) \frac{\partial \varepsilon}{\partial x_j} \right] \end{aligned} \tag{2.9}$$

The closure coefficient present in Equation 2.9 is detailed in table 2.1. These are considered universal and therefore constant in the k-ε model.

Table 2.1: Closure coefficients for the k-ε model.

C_μ	$C_{\epsilon 1}$	$C_{\epsilon 2}$	σ_k	σ_ϵ
0.09	1.44	1.92	1.00	1.30

The k-ε model was derived and tuned for flows with high Reynolds numbers [2]. Equation 2.8 and Equation 2.9 are independent when there is a separation of scales between the turbulent kinetic energy and the dissipation rate, which is the case for high Reynolds numbers [5]. For the model to remain valid through the viscous boundary layer near walls, either a low-Reynolds-number modification or the use of wall functions are required [2].

2.2.3 The k - ω Turbulence Model

In the k-ω model, the specific dissipation, ω, which is the inverse of the timescale on which the dissipation occurs, is used as the length determining quantity [2]. The transport equations for turbulent kinetic energy, k, and the specific dissipation rate are shown in Equations 2.8-2.11,

$$\frac{\partial k}{\partial t} + \langle v_j \rangle \frac{\partial k}{\partial x_j} = \nu_t \left[\left(\frac{\partial \langle v_i \rangle}{\partial x_j} + \frac{\partial \langle v_j \rangle}{\partial x_i} \right) \frac{\partial \langle v_i \rangle}{\partial x_j} \right] - \beta k \omega + \frac{\partial}{\partial x_j} \left[\left(\nu + \frac{\nu_t}{\sigma_k} \right) \frac{\partial k}{\partial x_j} \right] \tag{2.10}$$

$$\begin{aligned} \frac{\partial \omega}{\partial t} + \langle v_j \rangle \frac{\partial \omega}{\partial x_j} = \frac{\alpha}{k} \omega \nu_t \left[\left(\frac{\partial \langle v_i \rangle}{\partial x_j} + \frac{\partial \langle v_j \rangle}{\partial x_i} \right) \frac{\partial \langle v_i \rangle}{\partial x_j} \right] \\ - \beta^* \omega^2 + \frac{\partial}{\partial x_j} \left[\left(\nu + \frac{\nu_t}{\sigma_\omega} \right) \frac{\partial \omega}{\partial x_j} \right] \end{aligned} \tag{2.11}$$

where the turbulent viscosity, ν_t is calculated from Equation 2.12

$$\nu_t = \frac{k}{\omega}. \tag{2.12}$$

The values of the closure coefficients β, β^*, σ_ω and σ_k are presented in Table 2.2 [15].

Table 2.2: Closure coefficients for the k-ω model.

β	β^*	σ_ω	σ_k
0.09	0.075	0.5	0.05

In contrast to the k-ε model, the k-ω model does not require low Reynolds numbers or the use of wall functions [2]. This makes the k-ω model more favorable for accurately capturing the behavior of the viscous sublayer near walls, compared to the k-ε model. However, a very fine mesh is required close to the wall.

2.2.4 The SST k - ω Turbulence Model

The SST k-ω model combines the two turbulence models k-ε and k-ω, to utilize the strengths of both models [21]. The k-ε is used in free stream regions where it provides good accuracy, and the k-ω model is used in regions close to walls since it is good at predicting flow behavior near the boundary layer.

2.2.5 Turbulent Boundary Layers

At a solid wall, the no-slip condition is assumed, meaning that the relative velocity between the fluid and the wall is zero. [2]. Therefore, a boundary layer is formed, in which the velocity increases from zero at the wall to the free-stream velocity. Depending on the Reynolds number, such a boundary layer can be either laminar or turbulent. Turbulent boundary layers, occurring at high Reynolds numbers, feature swirling motions that enhance mass, momentum, and heat transfer, but also increase wall shear stress and drag. A turbulent boundary layer of thickness δ can be split into an outer region ($0.2\ \delta < \text{y} < \delta$) and an inner region ($0 < \text{y} < 0.2\ \delta$), where the latter can be further divided into:

$$y^+ = \begin{cases} 0 < y^+ \leq 5, & \text{Viscous sub-layer (laminar-dominated)} \\ 5 < y^+ \leq 30, & \text{Buffer sub-layer (transition zone)} \\ 30 < y^+ \leq 400, & \text{Logarithmic sub-layer} \quad \left(\frac{\nu}{\delta} = 0.1\text{–}0.2\right) \end{cases}$$

where $y^+ = \frac{y u_*}{\nu}$ is a scaled variable which describes the physical extent of the sub-layers. The division of the sublayers is based on the relative magnitude of the viscous and turbulent parts of the shear stress.

2.2.6 Wall Functions

To perform wall integration of turbulence models, the first computational cell must be located within the viscous sub-layer near the wall [12]. Therefore, a dense mesh is usually required to accurately resolve boundary layers in wall-bounded flows. An alternative to the dense mesh is wall functions, which may also be used to accommodate turbulence models that are not valid in the viscous near-wall region [2]. Wall functions reduce computational demand by, for instance, allowing the first cell to be placed in the logarithmic sub-layer, which significantly decreases the number of cells required near the wall [12]. The logarithmic theory of the wall is the theoretical basis behind wall functions. The main concept of wall functions is to avoid resolving the turbulence model in the near-wall region. This is done by applying the boundary conditions some distance away from the wall, typically at the first grid point P within the region where the wall function is valid [2]. The sharp velocity gradients close to the wall are thereby not directly resolved by the mesh, but instead approximated using empirical formulas, allowing for a coarser mesh without significantly compromising accuracy.

2.3 Volume of Fluid

The Volume of Fluid (VOF) method captures the interface between two immiscible fluids in an Eulerian framework [4]. This method uses a volume fraction to represent the two fluids while the interface is treated as a mixture. The indicator function, α, which is chosen to be the volume fraction, ranges from 0 to 1, where;

$$\alpha = \begin{cases} 0, & \text{control volume is only occupied by phase 1} \\ 0 < \alpha < 1, & \text{interface between the two fluids present} \\ 1, & \text{control volume is only occupied by phase 2.} \end{cases}$$

An additional transport equation is solved, simultaneously with the mass and momentum conservation equations, to capture the displacement of the interface. This transport equation is presented in Equation 2.13.

$$\frac{\partial \alpha}{\partial t} + \frac{\partial(\alpha \bar{v}_j)}{\partial x_j} = 0, \tag{2.13}$$

2.4 Stokes Wave Theory

Stokes wave theory is a non-linear gravity wave theory, which often serves as the basis for irregular wave modeling [4]. The theory entails using perturbation analysis to derive approximate solutions for periodic progressive waves of permanent form in intermediate and deep water. The theory describes that wave speed depends on wave amplitude and that periodic wavetrains can exist in non-linear systems.

The analysis starts with the potential flow formulation, using the Laplace Equation 2.14 to describe the flow's behavior and boundary conditions for free-surface kinematics and dynamics, described in Equation 2.15 [4],

$$\nabla^2 \phi = 0 \tag{2.14}$$

$$\cdot \frac{\partial^2 \phi}{\partial y^2} + g\frac{\partial \phi}{\partial z} + \frac{\partial}{\partial t}\left(\vec{u}\right)^2 + \frac{1}{2}\vec{u} \cdot \nabla u^2 = 0 \tag{2.15}$$

where ϕ is the velocity potential, and u is the fluid velocity. By expressing the boundary conditions as a Taylor series expansion about a free surface and choosing the constant elevation as $z = 0$, it guarantees that the expansion occurs in the proximity of the actual free surface elevation. The Taylor expansion gives the expression described in Equation 2.16,

$$\begin{multline}\left[\frac{\partial \phi}{\partial t} + g\frac{\partial \phi}{\partial z}\right]_0 + \eta\left[\frac{\partial}{\partial z}\left(\frac{\partial \phi}{\partial t} + g\frac{\partial \phi}{\partial z}\right)\right]_0 + \left[\frac{\partial}{\partial t}\left(\vec{u}\right)^2\right]_0 + \frac{1}{2}\eta^2\left[\frac{\partial^2 \phi}{\partial z^2}\left(\frac{\partial \phi}{\partial x^2} + g\frac{\partial \phi}{\partial z}\right)\right]_0 \\ + \eta\left[\frac{\partial^2 \phi}{\partial z^2}\left(\vec{u}^2\right)\right]_0 + \left[\frac{1}{2}\vec{u} \cdot \nabla \vec{u}^2\right]_0 + \cdots = 0 \end{multline} \tag{2.16}$$

where η is the free surface elevation, and g is gravity. Secondly, perturbation analysis is applied. By denoting a parameter $\epsilon = ka \leq 1$, where ka is the steepness of the wave, η, ϕ, and u can be expanded as described in Equation 2.17.

$$\eta = \epsilon\eta_1 + \varepsilon^2\eta_2 + \varepsilon^3\eta_3 ... + \varepsilon^n\eta_n \tag{2.17}$$

By inserting these expansions into the Laplace equation and Taylor expansion, different orders of approximation for the solution of the non-linear wave problem can be obtained [4]. With higher-order approximations, the complexity and number of terms increase. For waves modeled using Stokes wave theory, the speed depends on both amplitude and wavelength, in contrast to linear waves, where the speed is independent of these factors. Furthermore, Stokes waves have sharper peaks and shallower troughs, making them resemble real ocean waves more.

2.5 Scaling Laws for FOWTs

To enable model testing of FOWTs in testing facilities, the entire system must be scaled down to fit within the available space [7]. The hydrodynamic loads on FOWTs are primarily dominated by inertial forces and should therefore satisfy Froude scaling laws [6]. In contrast, the aerodynamic loads, which are predominantly influenced by viscous forces, should satisfy the Reynolds scaling laws. These scaling laws cannot be satisfied simultaneously, and since the motion response of FOWTs is influenced by the coupling of aerodynamic and hydrodynamic loads, this presents a significant challenge. Typically, models used in experimental model testing satisfy the Froude scaling laws, resulting in a relatively accurate representation of the hydrodynamic load, while compromising on the aerodynamics by only accounting for the major load components.

The Froude number represents the ratio between the magnitude of the inertial and gravitational forces in a fluid flow [6], as described in Equation 2.18,

$$F_r = \frac{v^2}{gL}, \tag{2.18}$$

where v is the fluid velocity, L is the characteristic length of the body in the fluid, and g is the gravitational acceleration. Froude scaling laws are based on the assumption that this number is identical for the model and the full scale, as shown in Equation 2.19 [9].

$$\frac{v_M^2}{gL_M} = \frac{v_F^2}{gL_F}, \tag{2.19}$$

Table 2.3 presents some important scaling ratios used to upscale a downscaled Froude model to its full scale, where $\lambda_s = \frac{L_F}{L_M}$.

Table 2.3: Froude Scaling Ratios for Various Parameters [9].

Parameter	**Dimension**	**Froude scale ratio**
	Geometric similarity	
Length	L	λ_s
Area	L^2	λ_s^2
Volume	L^3	λ_s^3
Rotation	–	1
	Kinematic similarity	
Time	T	$\lambda_s^{1/2}$
Velocity	LT^{-1}	$\lambda_s^{1/2}$
Acceleration	LT^{-2}	1
	Dynamic similarity	
Mass	M	λ_s^3
Force	MLT^{-2}	λ_s^3

3

Methods

This chapter describes the methods used for the simulations in this study, and is divided into the following sections:

- **Numerical Setup**: Describes the general numerical methods and simulation settings used across all cases.
- **Case 1 – Wave Simulations**: Describes small-scale wave simulations conducted to determine a setup capable of accurately capturing wave height and wave-induced currents.
- **Case 2 – Floater Simulations**: Describes full-scale simulations consisting of:
  - **Case 2.1 – Decay Test**: A free-decay simulation of the floater, compared to corresponding model test data.
  - **Case 2.2 – Regular Wave Test**: Simulations of the floater in regular waves were performed. A spatial and temporal resolution study was conducted, and the configuration that best balanced computational efficiency and accuracy was selected and validated against model test data.

3.1 Numerical Setup

Siemens STAR-CCM+ was used for geometry creation, mesh generation, and performing the simulations in this study. All simulations were executed on a high-performance computing (HPC) cluster utilizing two compute nodes. Each node featured a dual-socket configuration with AMD EPYC 9374F processors, each providing 32 physical cores, resulting in a total of 64 cores per node. All simulations were performed using the SST (Shear Stress Transport) k–ω turbulence model. This choice was made since the SST k–ω model has shown good performance in several previous studies, such as those conducted by Zhang et al. [23] and Wang et al. [20]. The multiphase flow was modeled using the Volume of Fluid method, which captures the interface between immiscible fluids within an Eulerian framework. To generate waves in the wave simulations, the VOF wave model was used. The VOF wave model is a special case of the VOF multiphase model for simulating surface gravity waves on the interface between a light and a heavy fluid [18]. Fifth-order Stokes waves were applied at the inlet boundary of the domain using a fifth-order approximation of the Stokes theory of waves, for which the wave profile and the wave phase velocity depend on the water depth, wave height, and current. Compared to the first-order waves, this model generates waves that more resemble real waves [20]. Furthermore, the use of first-order wave theory would give significant differences in the wave profile once the CFD computations are applied, due to its inability to capture nonlinear wave behavior. The turbulence specifications on the inlet and the outlet boundaries were the default values with an intensity of 0.01 and an viscosity ratio of 10.0 for all simulations. Furthermore, second-order temporal discretization was used. The segregated flow solver used the SIMPLE algorithm, with under-relaxation factors of 0.7 for the velocity and 0.3 for the pressure.

3.2 Case 1: Wave Simulations

To gain an understanding of wave simulation, a small domain was simulated. The primary objectives of this case were to accurately simulate the wave-induced current at the water surface and the wave height. The simulations were performed on a single compute node with 64 cores. The simulated 3D domain measured 10.5 m in length, 2.2 m in height, and a width of one base mesh cell. In this domain, a fifth-order Stokes wave with the characteristics described in Table 3.1 was imposed at the inlet as a boundary condition.

Table 3.1: Wave characteristics.

Parameters	Symbol	Value	Unit
Wave period	T	1	s
Wave height	H	0.06	m
Wave length	λ	1.58	m

To measure the water velocity, several point probes were positioned 4.8 meters downstream from the inlet, at various depths. The first point probe was placed at $z = -0.03$ m depth. From there on, point probes were placed at intervals of 0.02 meters down until $z = -0.33$ m. Additionally, two point probes were positioned at $z = 0.4$ m and $z = -0.8$ m, respectively. This is visualized in Figure 3.1. Point probes were also placed at the same depths at the domains inlet to ensure that the generated waves had the correct characteristics. It should be noted that the waves propagated in the positive x-direction in Case 1.

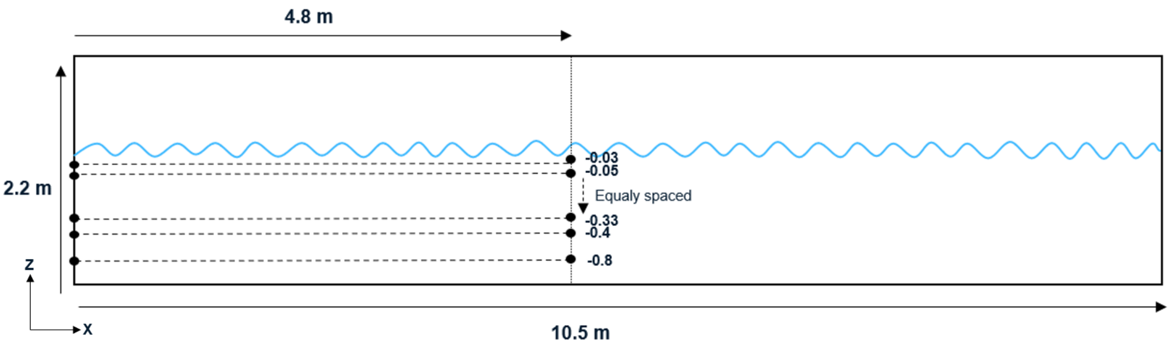

Figure 3.1: Wave simulation domain with visualized probe points.

The mesh was created using the trimmer meshing tool, which generates hexahedral cells, as well as the surface remesher tool. At the bottom of the domain, Prism Layer Mesher was used to create four prism layers, with a total thickness of one base mesh size, with a prism layer stretching of 1.4, as visualized in Figure 3.2. Based on the STAR-CCM+ guidelines regarding VOF waves, a volumetric custom control was used to refine the mesh around the water surface to accurately capture the behavior of the wave, as illustrated in Figure 3.3. The guidelines state targets regarding the number of cells per wave height and wave length within this mesh refinement. In the software, all cell dimensions must be either equal to or a power-of-two multiple of the smallest cell dimension (e.g., 2, 4, 8, 16 times the smallest size). This constraint makes it difficult to achieve the target number of cells for both the wave height and the wavelength simultaneously. The volumetric custom control covered the entire domain in the x- and y-direction, and in the z-direction, it was 2.2 times the wave height, enclosing the entire wave. The time step used was $\Delta t = 0.002$ s.

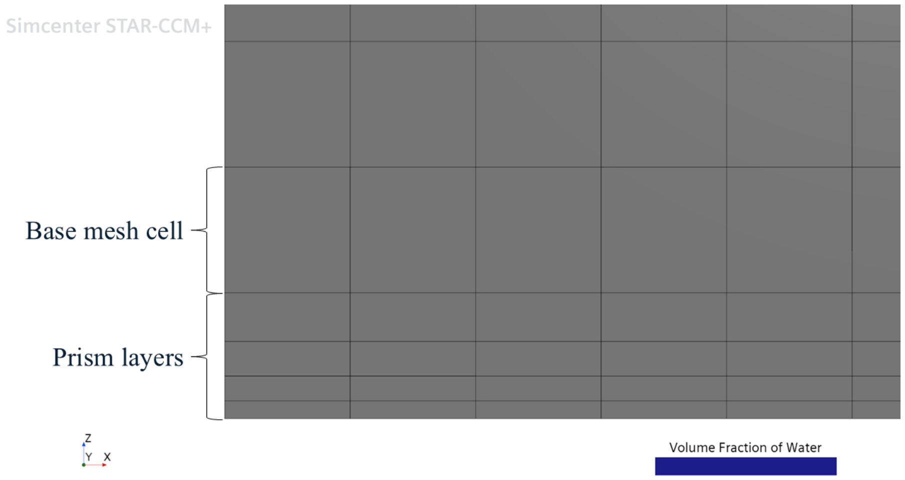

Figure 3.2: Prism layers and base mesh for Case 1.

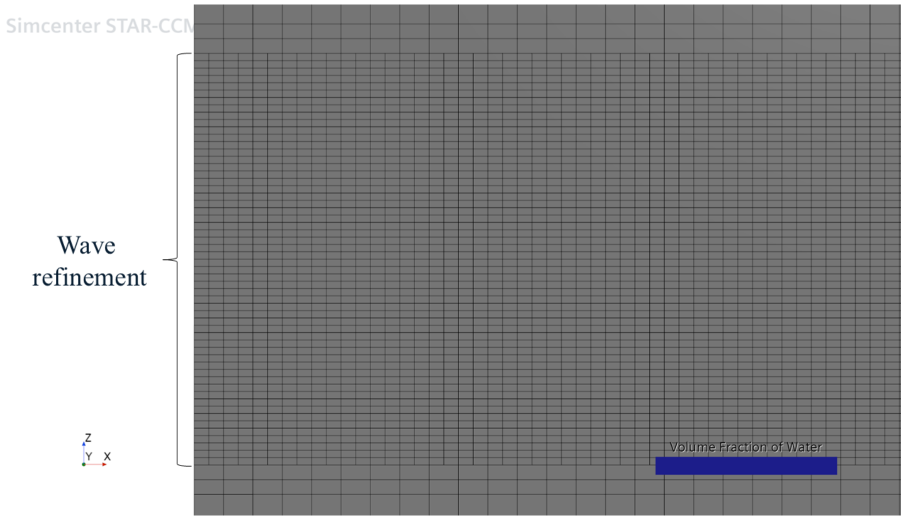

Figure 3.3: Mesh wave refinement for Case 1.

A mesh study was performed on the domain, focusing on capturing the mean water velocity and wave height correctly. The meshes investigated are described in Table 3.2, where z and x describe the size of the cells within the wave refinement, and *base* describes the size of the cells in the base mesh.

Table 3.2: Specification of grids used for the mesh study for Case 1.

Base mesh comparison	Base mesh cell size [m]
$z = 0.003$ $x = 4z$ $base = 16z$	0.048
$z = 0.003$ $x = 4z$ $base = 8z$	0.024
$z = 0.003$ $x = 4z$ $base = 4z$	0.012
Cells per wave λ comparison	Cells per λ
$z = 0.003$ $x = 8z$ $base = 16z$	66
$z = 0.003$ $x = 4z$ $base = 8z$	132
$z = 0.003$ $x = 2z$ $base = 4z$	264
Cells per wave H comparison	Cells per H
$z = 0.012$ $x = 2z$ $base = 4z$	5
$z = 0.006$ $x = 2z$ $base = 4z$	10
$z = 0.004$ $x = 2z$ $base = 4z$	15
$z = 0.003$ $x = 2z$ $base = 4z$	20
$z = 0.0024$ $x = 2z$ $base = 4z$	25
$z = 0.002$ $x = 2z$ $base = 4z$	30

Slip wall boundary conditions were set for the two boundaries on the sides of the domain, as well as for the top. The bottom of the domain was specified as a no-slip wall. The inlet was specified as a velocity inlet, where the velocity is evaluated using the field function of the velocity of the specified fifth-order VOF wave. Furthermore, one wavelength of wave forcing was applied at the inlet to force the waves to follow the Stokes fifth-order wave theory. The outlet was specified as a pressure outlet with one wavelength of wave forcing, where the pressure was defined as the field function for the hydrostatic pressure of the heavy fluid (water) of the fifth-order wave.

In Case 1, each simulation was run for a simulated duration of 20 seconds, corresponding to 20 wave periods. The mean water velocities in the x-direction over the final five wave periods were calculated for each point probe. To facilitate comparison, these mean velocities were converted into mean volume flow rates per meter. This was achieved by multiplying each positive mean water velocity by the vertical distance to the point probe directly beneath it. The resulting positive products were then summed to yield the total volume flow rate in the positive x-direction per meter over the last five wave periods. An example of these calculations for one of the simulations is presented in Appendix A. Additionally, the wave height of the final wave was extracted at $x = 4.8$. This value was then divided by the input wave height used in the simulations to quantify the deviation.

3.3 Case 2: Floater Simulations

The floater simulations consisted of two parts: Case 2.1, which involved a decay test simulation, and Case 2.2, which comprised simulations of the floater in regular waves. The simulation in Case 2 were all run on 2 nodes, equal to 128 CPU cores. For the simulations in Case 2, a rectangular cuboid domain was generated, pictured in Figure 3.4. The domains dimensions were based on the water depth, floater width and wave length, as described in Table 3.3. Furthermore, the still water surface coincided with $z = 0$.

Table 3.3: The dimensions of the computational domain used in Case 2.

W [m]	L [m]	H [m]
6xFloater width	5λ	1.5xWater depth

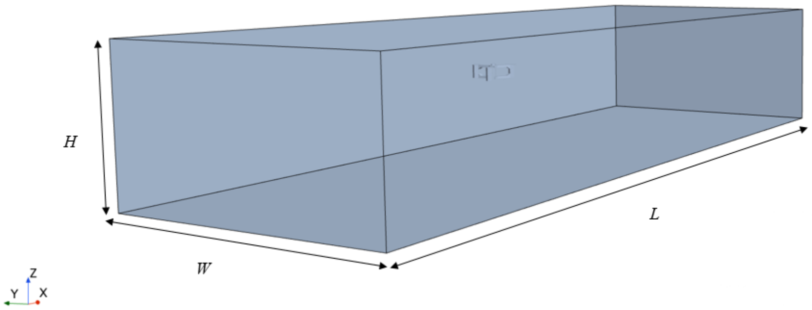

Figure 3.4: The computational domain used in Case 2.

The floater geometry was created using the 3D-CAD model in STAR-CCM+, based on the provided dimensions from Aker Solutions. Furthermore, the floater's center of gravity was aligned with $x = 0$ and $y = 0$. The geometry is visualized in Figure 3.5. In the model test, the floater geometry was constructed at model scale, whereas in the simulations, the floater was modeled in full scale. Hence, the model test data used for comparison in the following subsections was scaled up to full scale using Froude scaling, as described in Section 2.4.

Figure 3.5: Floater geometry.

For Case 2.2, all boundary conditions were defined in the same manner as described in Section 4.1 for Case 1, and are summarized in Table 3.4. For Case 2.1, the only differences in boundary conditions from the other cases were that the inlet velocity was prescribed using the field function corresponding to a flat VOF wave, and the pressure at the outlet was calculated using the field function for the hydrostatic pressure of the heavy fluid (water) associated with the flat VOF wave.

Table 3.4: Summary of boundary conditions used for Case 2.

Boundary	Type	Forcing/Damping
Inlet	Velocity Inlet	1λ Forcing
Outlet	Pressure Outlet	2λ Damping
Bottom	No Slip Wall	-
Top	Slip wall	-
Side 1	Slip wall	-
Side 2	Slip wall	-

For Case 2.1 and Case 2.2, a base mesh, with a reference cell size $h = 0.95$ m, was created based on the results from Case 1 and the STAR-CCM+ VOF wave guidelines [18]. The mesh was created with four refinement zones with different mesh sizes, as described in Table 3.5. As previously mentioned, the STAR-CCM+ VOF wave guidelines state that there should be a refinement zone that covers the wave region, ensuring that the mesh can resolve both the amplitude and the wavelength [18]. This mesh refinement is denoted zone 1. The mesh was created using the trimmer meshing tool, which generates hexahedral cells, and the surface remesher tool. At the bottom of the domain, Prism Layer Mesher was used to create four prism layers, with a total thickness of one cell in zone 2. Zone 4 covers the floater with a few meters of marginal in each direction. In zone 4, the cell size in the x-direction was reduced to make sure that the floater's motion could be captured correctly. The mesh is visualized in Figure 3.6.

Table 3.5: Description of the base mesh's refinement zones in Case 2.

Zone	y [m]	x [m]	z [m]	$\Delta y/h$	$\Delta x/h$	$\Delta z/h$
1	Full-span	Full-span	[-0.65H, 0.65H]	2	4	1
2	Full-span	Full-span	[-Water depth, -0.65H]	4	4	4
3	Full-span	Full-span	[0.65H, 0.5× Water depth]	4	4	4
4	[-50, 60]	[-60, 60]	[-19, 22]	2	2	1

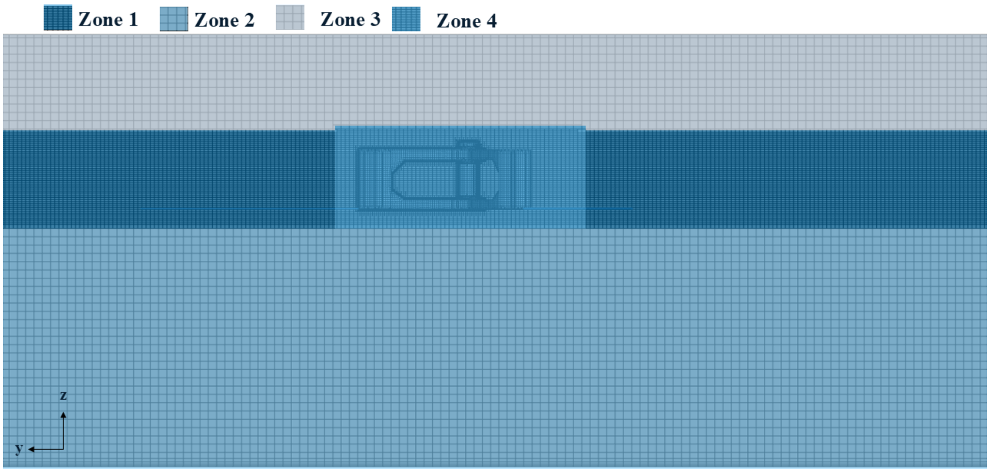

Figure 3.6: The base mesh used for Case 2 with visualization of the refinement zones.

To simulate the motion of the floater, the Dynamic Fluid Body Interaction (DFBI) approach was used in combination with the morphing mesh approach. Furthermore, the floater was set as a continuum body. The DFBI approach enables simulations of a rigid 6-DOF body's motion, accounting for the displacement and rotation caused by mechanical and multiphysics interaction [18]. For a 6-DOF body, its motion can be described by tracking the translation of a single point and the rotation around it. This point is usually the center of mass, and the relative motion of any other part of the body can be determined from it. The morphing mesh approach accounts for the effect of moving boundaries by redistributing mesh vertices in response to the movement of a set of control points in a transient simulation. This allows the mesh to deform in response to movement of a boundary, without having to re-mesh.

3.3.1 Case 2.1: Decay Simulation

To validate the floater geometry, a roll decay test was simulated and the results were compared to model decay test data. A decay test is an experimental method used in marine engineering and offshore engineering to estimate the eigen periods and hydrodynamic coefficients of a floating structure [13]. For a FOWT, such experiments are conducted by displacing the floater from its equilibrium position in the DOF of interest. When the floater is released, it oscillates with its eigen period in that DOF. The model basin decay test was conducted using a downscaled setup, and the results were subsequently scaled up. The wave model was set to flat waves, creating still water conditions in the previously described domain. Initially, the floater was tilted until reaching the displacement used in the decay model test. After obtaining the desired displacement, the floater was released and allowed to oscillate for several eigenperiods. The initial displacement of the floater is displayed in Figure 3.7. In the model test, the initial displacement of the floater was achieved by manually pulling the tower and simultaneously pressing down on the floater using a pole.

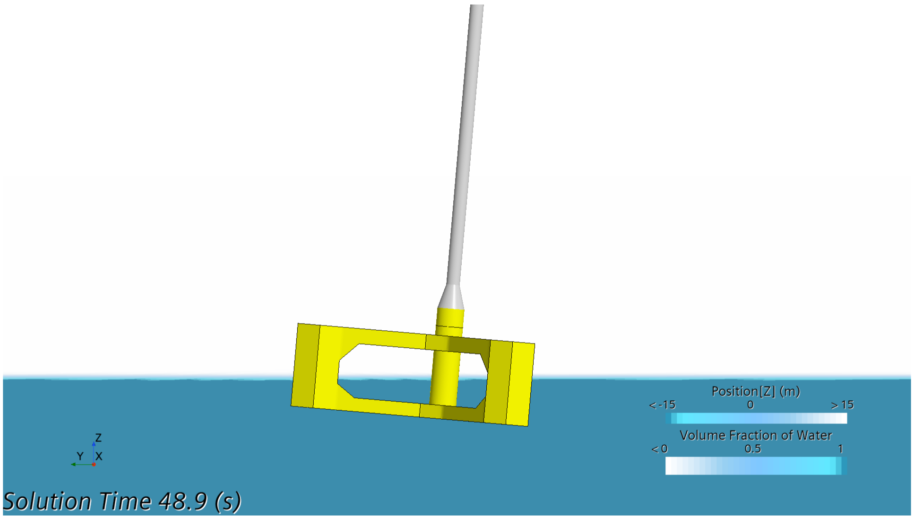

Figure 3.7: The initial displacement of the floater in the decay test in Case 2.1.

3.3.2 Case 2.2: Floater Wave Simulations

The response of the floater under regular wave conditions was simulated to compare with a model test. The model test was conducted using a downscaled setup, and the results were subsequently scaled up. The characteristics of the fifth-order Stokes waves are listed in Table 3.6.

Table 3.6: Wave characteristics of the fifth-order Stokes waves in Case 2.2.

Parameters	Symbol	Value	Unit
Wave period	T	13.9	s
Wave height	H	19	m
Wave length	λ	310	m

The DFBI approach, previously described in Section 3.3, enables the addition of body couplings. This feature was used to add mooring lines to the floater. The mooring system in the model test was based on catenary lines. This mooring system would be very challenging to model in STAR-CCM+, due to the complex design of the catenary lines. Hence, a simplified mooring system was implemented, consisting of three horizontal spring-dampers, one at the bottom of each of the three outer columns, as visualized in Figure 3.8. The input data required for the mooring system was provided by Aker Solutions. This included the elastic coefficient, relaxation length and elongated length of the spring dampers. The simplified mooring system was considered to provide representative dynamic results, but deviations in mean values were expected compared to the model test.

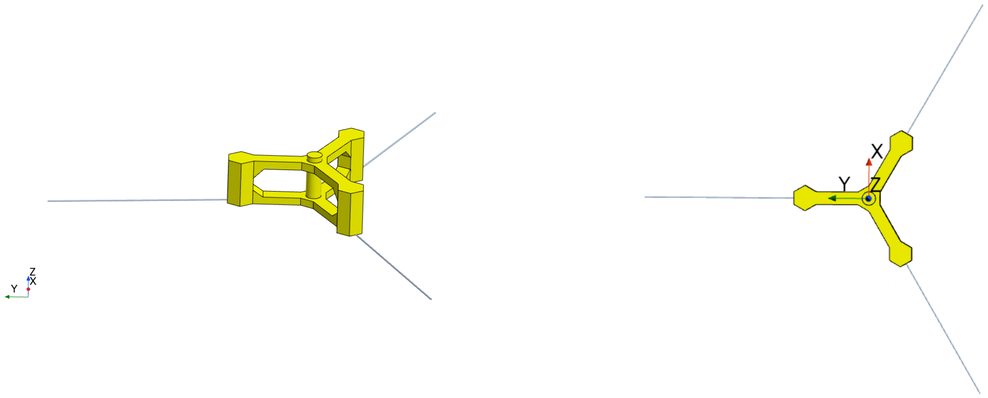

Figure 3.8: The mooring system used in Case 2.2.

To minimize the number of cells while ensuring mesh independence, a spatial discretization study was conducted using four different mesh resolutions, as described in Table 3.7. A time step of Δt=0.02 seconds with 10 inner iterations was used for these simulations. The wave period in the simulations was 13.9 s, and with a time step of Δt=0.02s, this corresponds to approximately 695 time steps per wave period (13.9/0.02=695). This provided a high temporal resolution, ensuring accurate capture of the wave motion and the floater's dynamic response. Mesh 1, which was the finest mesh, was used as a reference simulation, which was run for 400 seconds. For this simulation, the time series of the results were extracted. Based on the results of the reference simulation presented in Section 4.2.2.1, the rest of the simulations in the spatial discretization study were run for 10 wave periods, equal to 139 seconds. The parameters evaluated included the positions in the y- and z-directions, rotation around the x-axis, and wave height. The wave probe where the wave height was measured was placed before the waves reached the floater, roughly one floater width away from the floater in negative x-direction and positive y-direction, as described in Figure 3.9. It should also be noted that the waves propagated in the negative y-direction. The y-position was measured relative to the floater's center of gravity, while the z-position was measured relative to the water surface. For each of the parameters, the maximum and minimum values from the final wave period were extracted. These values were then used to calculate the amplitude for all parameters. For the position in the y-direction, position in the z-direction, and rotation around the x-axis, the mean values were also computed. The mean was taken as the average of the final maximum and minimum, and the amplitude was calculated using Equation 3.1.

$$\text{Amplitude} = \frac{\text{Max} - \text{Min}}{2} \tag{3.1}$$

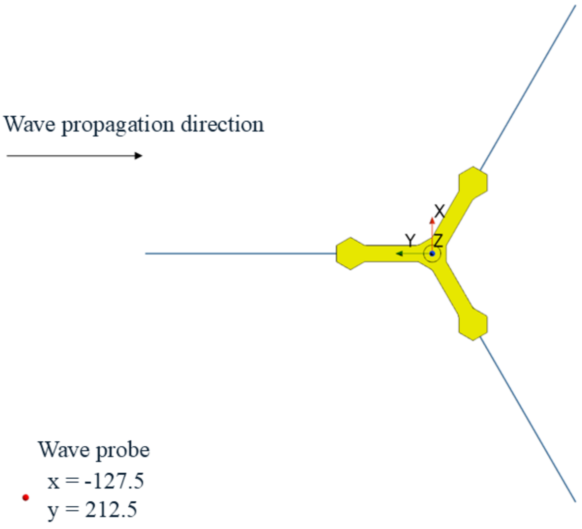

Figure 3.9: Visualization of the wave propagation direction and the wave probe placement in Case 2.2.

Table 3.7: Description of meshes used for the spatial discretization study in Case 2.2.

Mesh	Cells per H	Cells per λ	Nr of cells
1	20	164	7,181,701
2	15	123	3,031,158
3	10	164	1,657,458
4	5	82	236,615

To further reduce the computational time without compromising the accuracy of the results, a temporal discretization study was also conducted. The investigated time step sizes are described in Table 3.8. These simulations were run over the same duration as those in the spatial discretization study, and the results were evaluated using the same methodology.

Table 3.8: Description of the temporal discretizations used for the temporal discretization study in Case 2.2.

Discretization	Time step [s]	Inner iterations
1	0.005	10
2	0.01	10
3	0.02	10
4	0.04	10

After the spatial and temporal discretization studies were conducted, the results of the best simulation were compared to the model test data. The model test data were extracted after the system reached a periodic state and were aligned with the corresponding periodic state of the reference simulation.

4

Results and Discussion

The results and the discussion of the simulations described in chapter 3 are presented in this chapter. This includes the results and discussion for Case 1, Case 2.1 and Case 2.2.

4.1 Case 1: Wave domain

Figures 4.1-4.6 display the results of Case 1, in the form of comparisons of the results of simulations performed with different mesh refinements. In Appendix A, the calculation of the mean water flow for the simulation with $z = 0.024$, $x = 2z$, and $base = 4z$ is shown in detail (see Table A.1 and Figure A.1). Furthermore, all numerical values of the results from Case 1 are summarized in Table A.2 in Appendix A.

Figures 4.1-4.2 compares the results for simulations with different base sizes. From Figure 4.1, it is evident that doubling the size of the base mesh from $base = 4z$ to $base = 8z$ does not significantly impact the mean water flow. However, doubling the base size from $base = 8z$ to $base = 16z$ increases the mean water flow considerably. This indicates that $base = 8z$, equal to 0.024 m, is enough to capture the mean water flow. The wave height for the three simulations all deviates less than 1%, as demonstrated in Figure 4.2. This indicates that the base mesh size does not impact the wave height. Hence, a base size of $base = 16z$, equal to 0.048 m, is enough to capture the wave height.

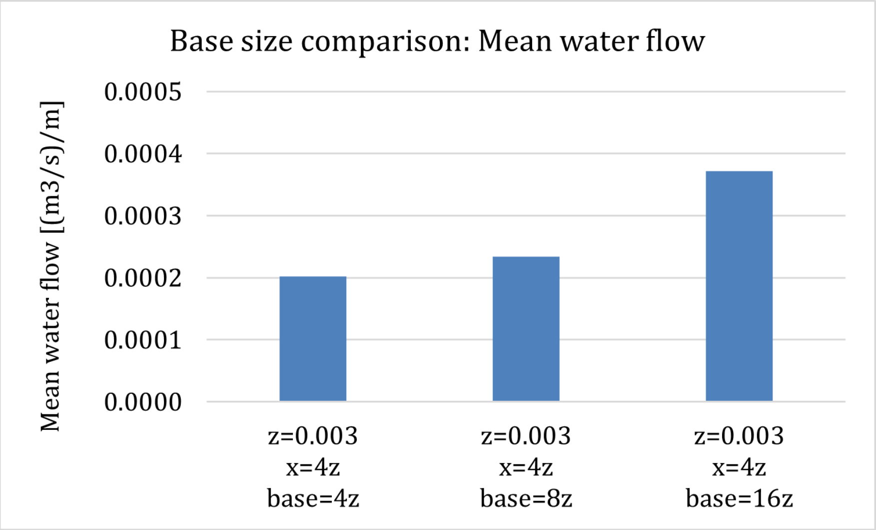

Figure 4.1: Comparison of the total mean water flow in positive x-direction at $x = 4.8$ m for different base mesh sizes.

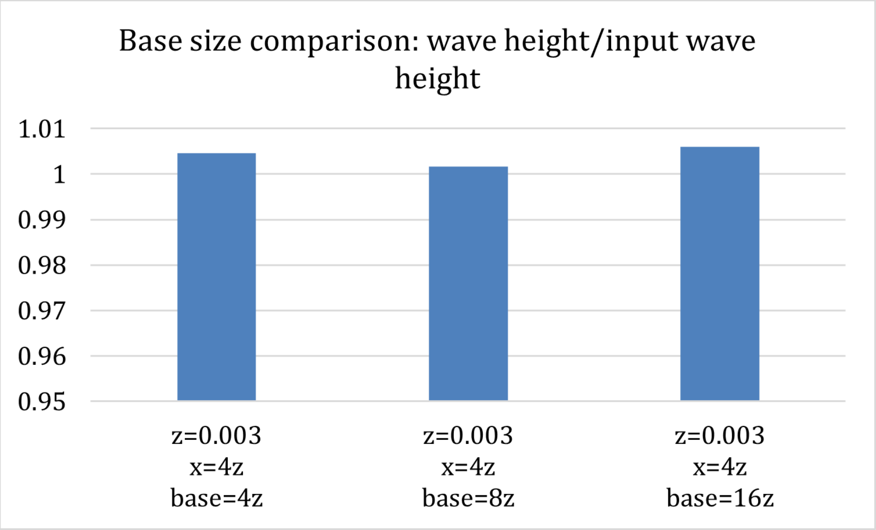

Figure 4.2: Comparison of the wave height at $x = 4.8$ m in relationship to the specified wave height for different base mesh sizes.

Figures 4.3-4.4 compares the results of simulations with different cell sizes in the x-direction within the wave refinement. The difference in mean water flow between $x = 2z$ and $x = 4z$ is very small, as demonstrated in Figure 4.3. In contrast, $x = 8z$ results in a mean water flow more than four times greater than the mean water flows of $x = 2z$ and $x = 4z$. A similar pattern is observed in Figure 4.4, where the wave height for $x = 8z$ differs from the other two sizes by about 3%. Based on these results, it can be concluded that $x = 4z$, corresponding to 132 cells per wavelength, is enough to capture the mean velocity and the wave height.

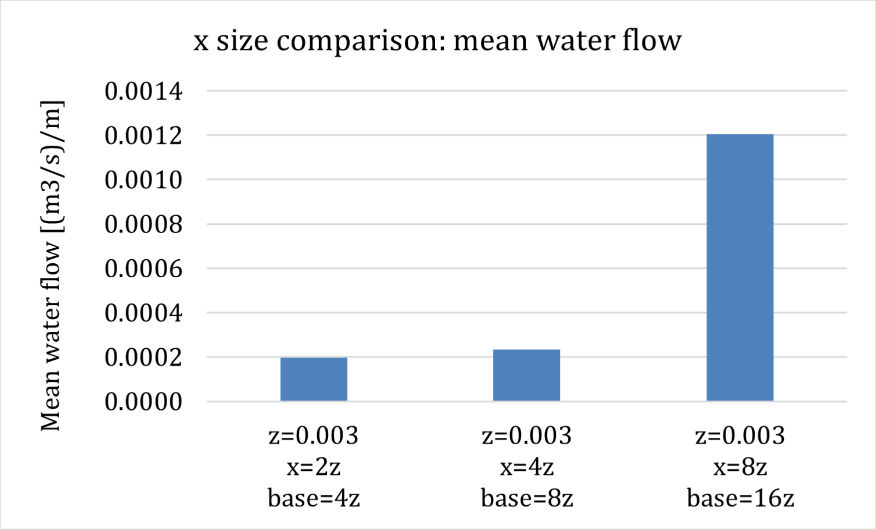

Figure 4.3: Comparison of the total mean water flow in positive x-direction at $x = 4.8$ m for different mesh sizes in the x-direction in the wave mesh refinement.

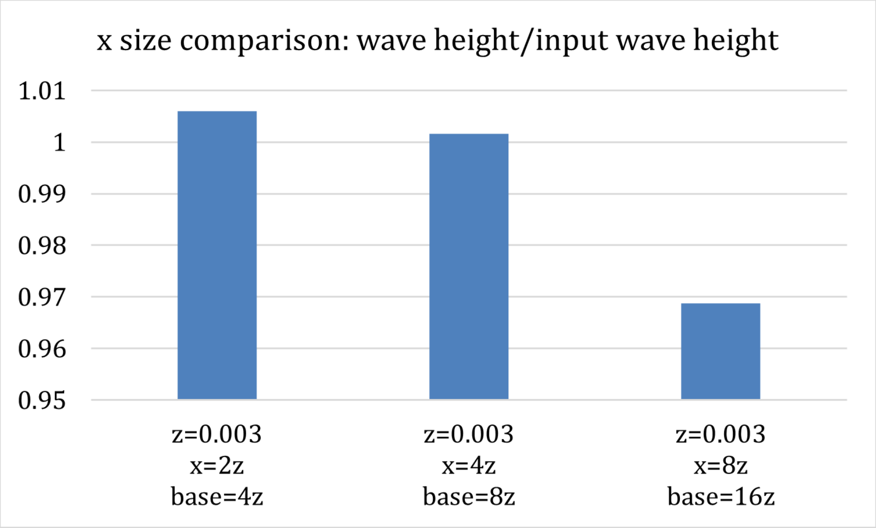

Figure 4.4: Comparison of the wave height at $x = 4.8$ m in relationship to the specified wave height for different mesh sizes in x-direction in the wave mesh refinement.

Figures 4.5 -4.6 compare the results of simulations with different cell sizes in the z-direction within the wave refinement zone. From Figure 4.5, it can be seen that the mean water flow varies significantly with cell size in the z-direction. Only the second finest cell size, $z = 0.0024$ m, yields results comparable to those of the finest cell size, $z = 0.002$ m. Therefore, to capture the mean water flow, a cell size of $z = 0.0024$ m, corresponding to 25 cells per wave height, is required. All cell sizes of z except $z = 0.012$ generate wave height differing less than 1% from the input wave height. Consequently, a cell size of $z = 0.006$ m, equivalent to 10 cells per wave height, is satisfactory to capture the wave height.

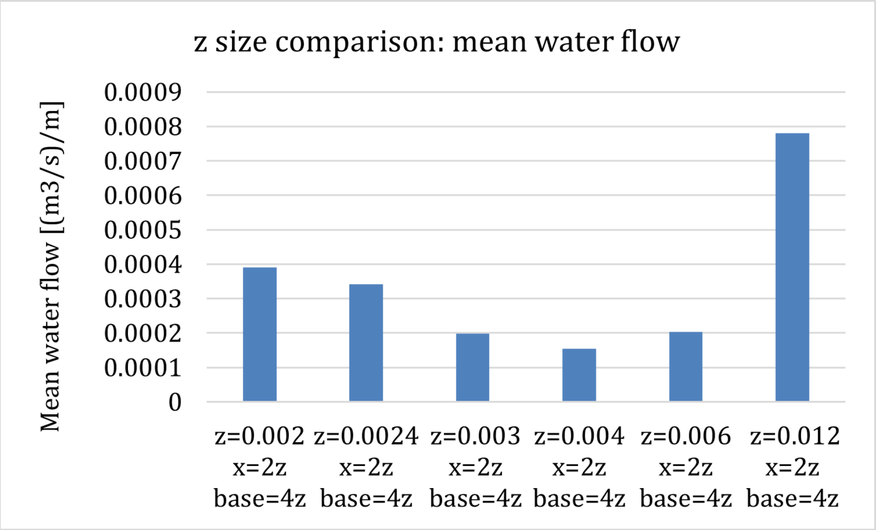

Figure 4.5: Comparison of the total mean water flow in positive x-direction at $x = 4.8$ m for different mesh sizes in z-direction in the wave mesh refinement.

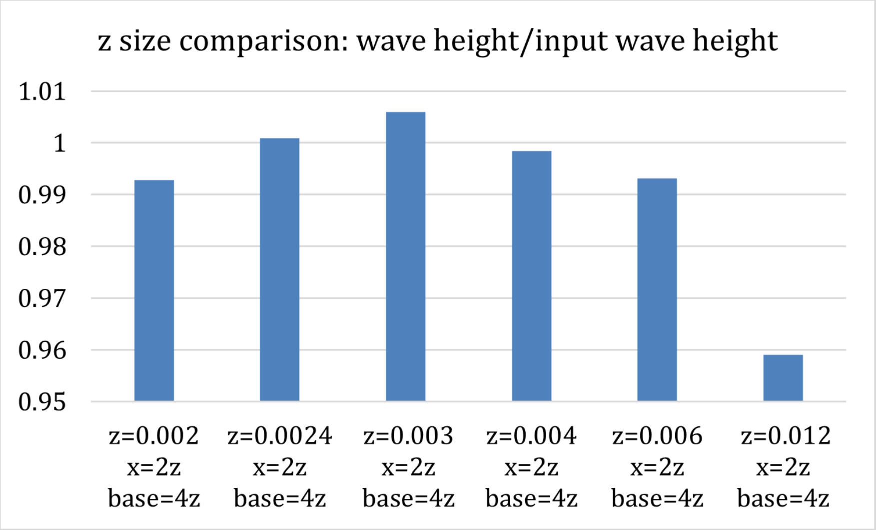

Figure 4.6: Comparison of the wave height at $x = 4.8$ m in relationship to the specified wave height for different mesh sizes in the z-direction in the wave mesh refinement.

To summarize, a mesh with at least 25 cells per wave height and 132 cells per wave length, within the wave refinement zone, is required to capture the mean water flow. Furthermore, the base mesh size should not exceed the cell size in the z-direction within the wave refinement zone. The mesh required to capture the wave height is significantly coarser, with 10 cells per wave height, 132 cells per wave length, and a base mesh size of 16 times the cell size in the z-direction within the wave refinement zone.

4.2 Case 2: Floater simulations

The simulations results in Case 2 consist of two parts: Case 2.1, which involves the decay test simulations, and Case 2.2, which focuses on the floater simulations in waves.

4.2.1 Case 2.1: Decay simulations

The results of the decay test in Case 2.1 are presented in Figure 4.7 and Figure 4.8. Figure 4.7, which depicts the time series of the floater's rotation around the x-axis, reveals that the simulation results exhibit an increasing phase shift relative to the model test results over time. Although the shift with time becomes very evident, the deviation in period time for each of the first 10 oscillations is less than 4.6 %, as exhibited in Figure 4.8. As the results align reasonably well with the model test data, it can be concluded that the center of gravity is in the correct place and that the moment of inertia and mass are of the correct magnitude. Furthermore, the similar reduction of the amplitude of the rotation over time indicates that the damping of the simulated floater is correct. As described in Section 3.3.1, the initial displacement of the floater in the model test is achieved manually. This means that there are some uncertainties in the methodology, which could explain the small deviations in the results.

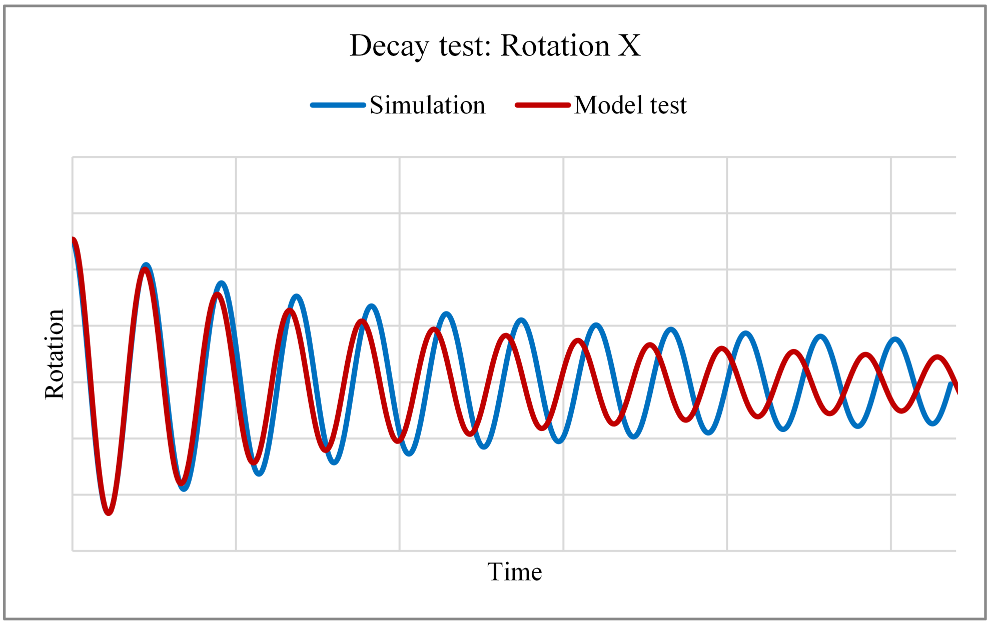

Figure 4.7: Comparison of the floater's rotation around the x-axis between the simulated decay test and the model decay test.

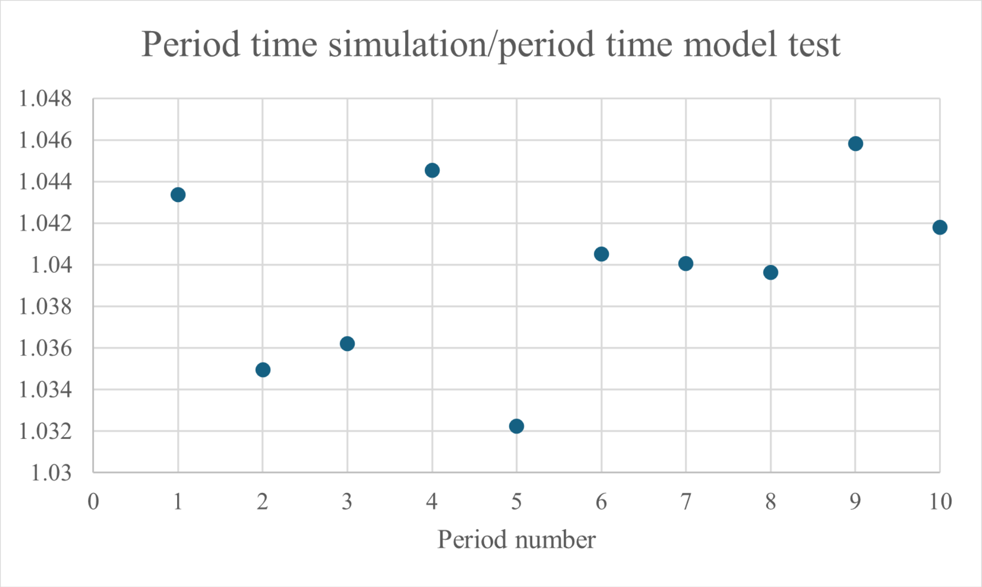

Figure 4.8: Comparison of the floater's rotation around the x-axis between the simulated decay test and the model decay test.

4.2.2 Case 2.2: Floater wave simulations

4.2.2.1 Reference simulation

The reference simulation results are presented in the format of time series, displayed in Figures 4.9-4.12. After about 130 seconds, the results obtain a periodic state. Therefore, it can be considered reasonable to extract the values corresponding to the last observed maximum and minimum before 139 seconds for the four investigated parameters. The extracted maximum and minimum values are marked in the figures. In Equations 4.2-4.6, it is described how the amplitude and mean position of the floater in y- direction and rotation around the x-axis, the amplitude of the floater's position in z-direction and the wave height, were calculated.

$$\text{Amplitude position y} = \frac{(-4.6\,\text{m}) - (-18.8\,\text{m})}{2} = 7.05\,\text{m} \tag{4.1}$$

$$\text{Mean position y} = \frac{(-4.6\,\text{m}) + (-18.8\,\text{m})}{2} = -11.7\,\text{m} \tag{4.2}$$

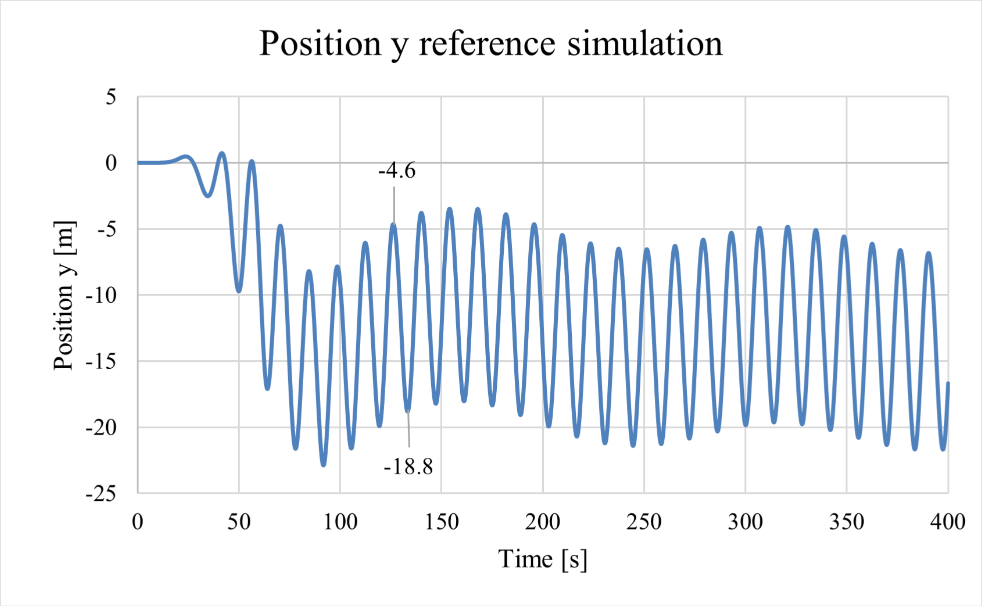

Figure 4.9: Time series of the floater's position in y-direction for the reference simulation in case 2.2.

$$\text{Amplitude position z} = \frac{(7.6\,\text{m}) - (-8.4\,\text{m})}{2} = 8\,\text{m} \tag{4.3}$$

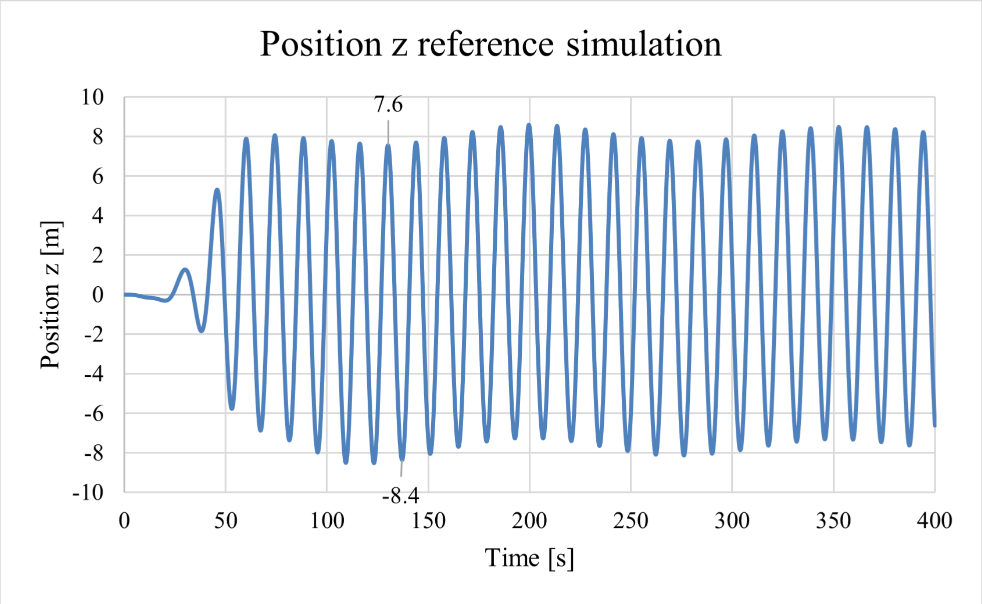

Figure 4.10: Time series of the floater's position in z-direction for the reference simulation in case 2.2.

$$\text{Amplitude rotation x} = \frac{(4\,\text{degrees}) - (-4.9\,\text{degrees})}{2} = 4.45\,\text{degrees} \tag{4.4}$$

$$\text{Mean rotation x} = \frac{(4\text{ degrees}) + (-4.9\text{ degrees})}{2} = -0.45\text{ degrees} \tag{4.5}$$

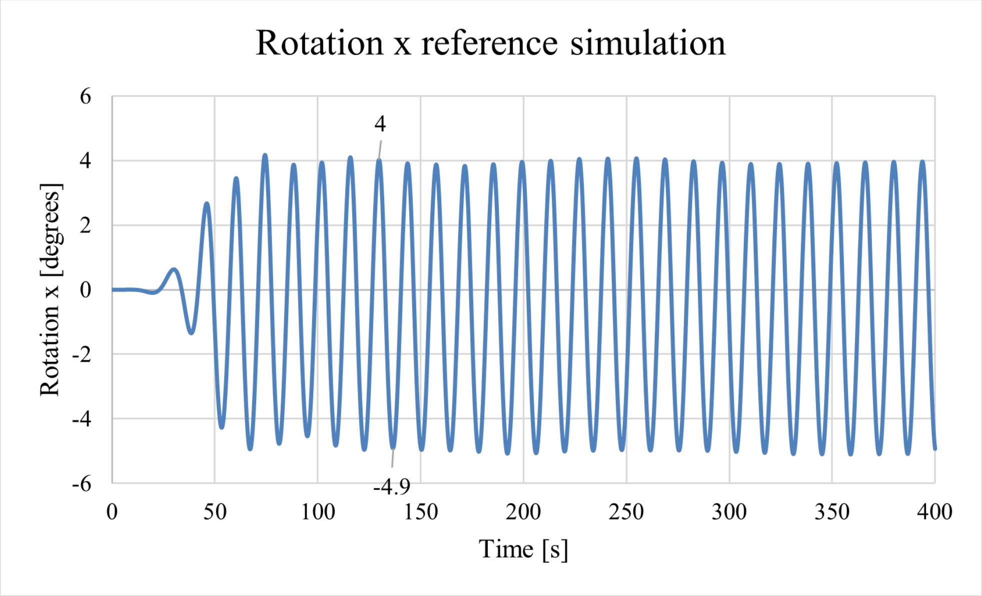

Figure 4.11: Time series of the floater's rotation around the x-axis for the reference simulation in case 2.2.

$$\text{Wave height} = (9.5\text{ m}) - (-8.8\text{ m}) = 18.3\text{ m} \tag{4.6}$$

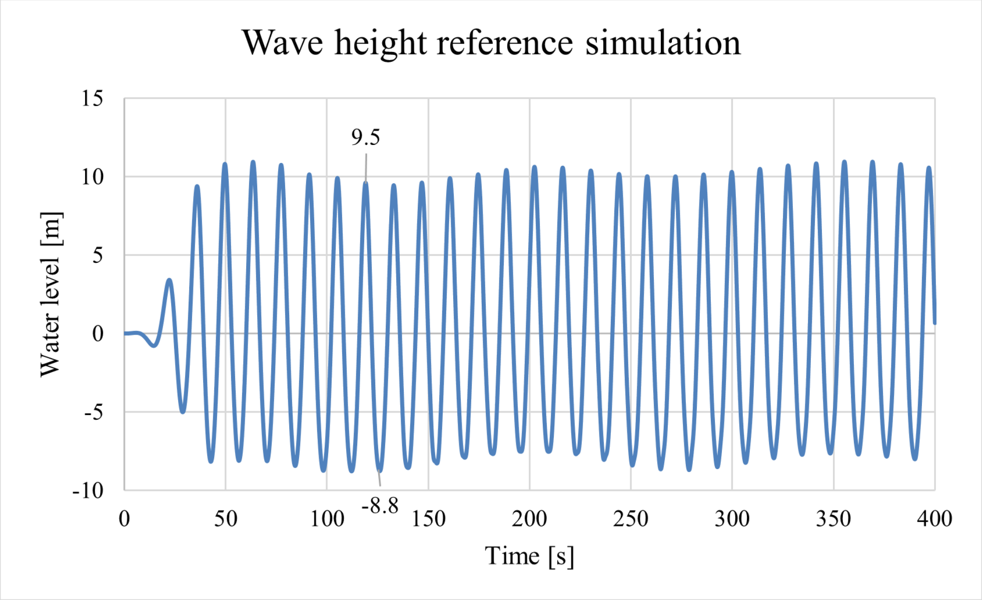

Figure 4.12: Time series of the wave height for the reference simulation in case 2.2.

The floater's motion over a 10-second period in the reference simulation is visualized in Figure 4.13.

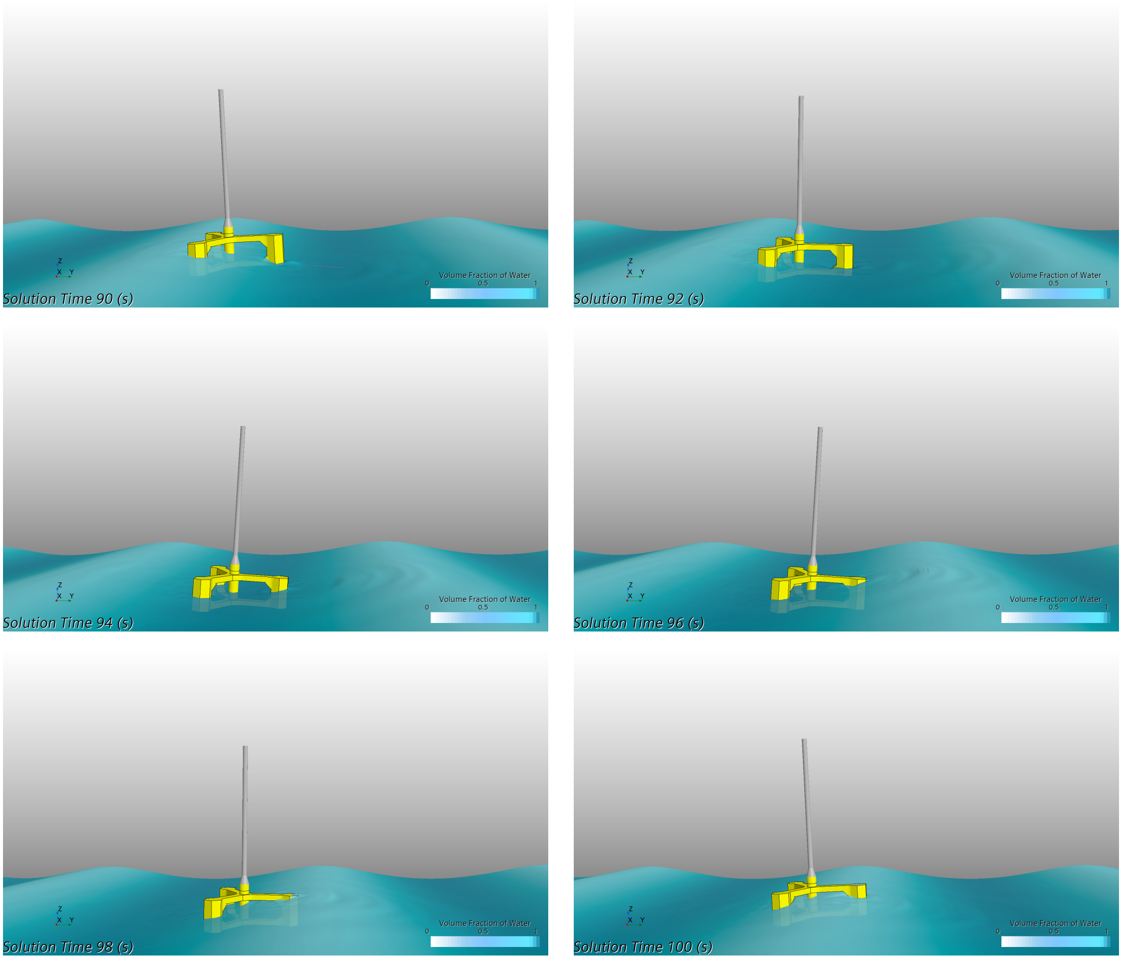

Figure 4.13: Visualization of the floater's movement in waves for the base simulation.

4.2.2.2 Spatial and Temporal Discretization Studies

Figures 4.14–4.17 present the results of the spatial discretization study. Furthermore, the computational time required for each simulation is shown in Figure 4.18.

The results of the spatial study, regarding the position in y-direction of the floater's center of gravity, are displayed in Figure 4.14. From the results, it is evident that the amplitude of the position y is barely affected by the reduction from 20 to 15 cells per wave height. Furthermore, the results for 10 and 5 cells per wave height are very close to the results of the previously mentioned. In contrast, the mean position in the y-direction shows significantly more variation across the different mesh resolutions, particularly for the coarser grids. This suggests that while the amplitude remains rather constant, the baseline position may be more sensitive to mesh refinement.

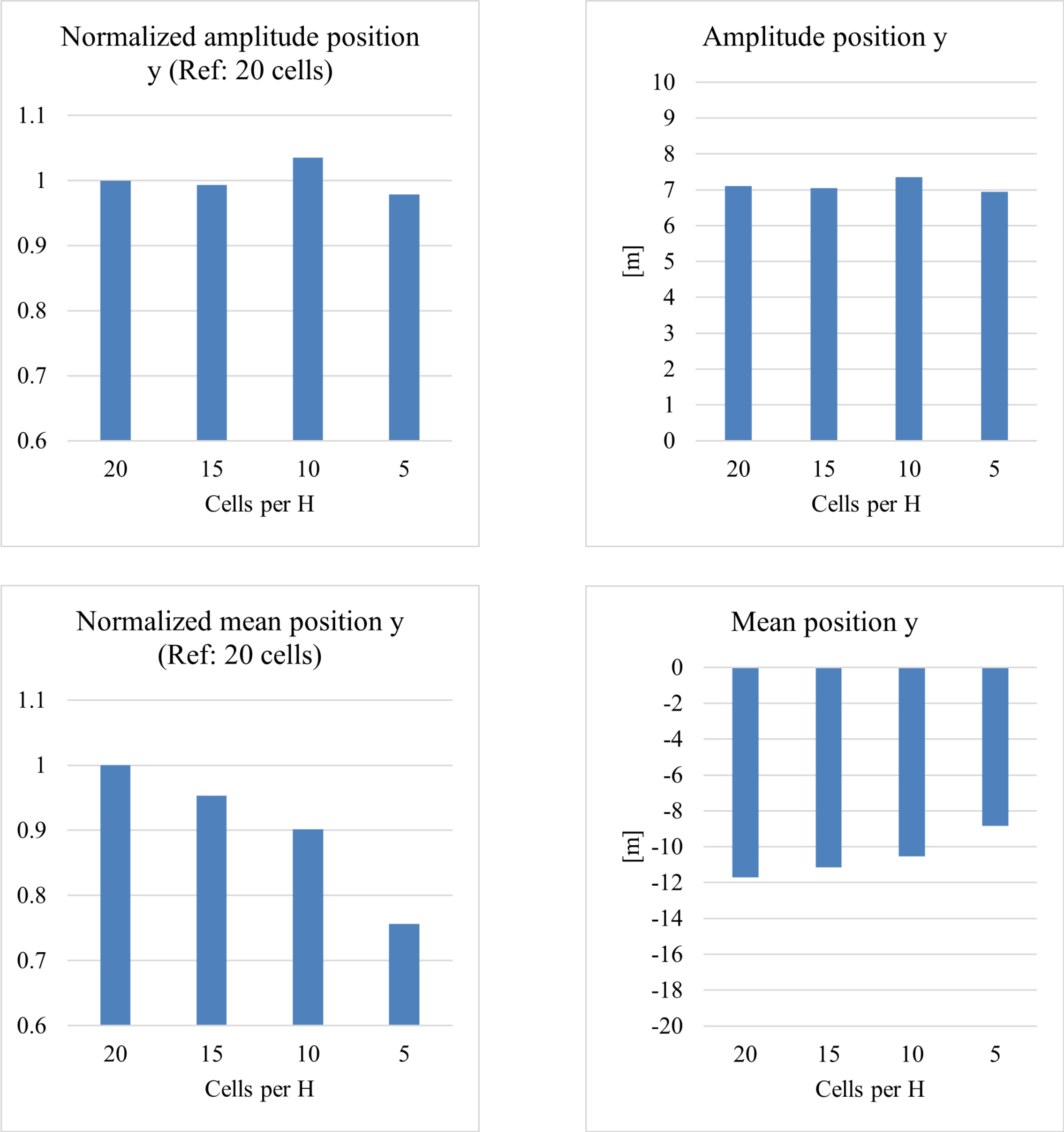

Figure 4.14: Comparison of normalized and actual amplitudes and mean values of the position of the floater's center of gravity in the y-direction for the spatial study.

Figure 4.15 visualizes the results of the spatial discretization study regarding the position in the z-direction of the floater's center of gravity. The amplitude of the z-position varies by less than 3% across the four mesh resolutions. Moreover, the mean position in the z-direction is also minimally affected by the mesh refinement.

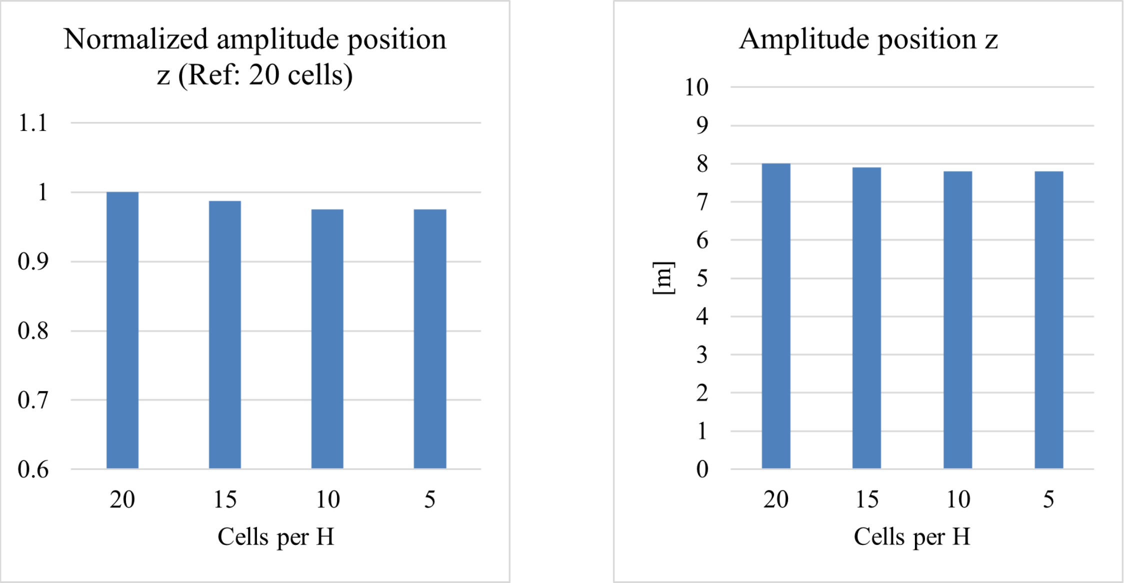

Figure 4.15: Comparison of normalized and actual amplitudes of the floater in the z-direction for the spatial study.

The results concerning the floater's rotation around the x-axis, commonly called roll, are presented in Figure 4.16. A comparison of both the normalized and the actual roll amplitudes for the different mesh resolutions reveals that the amplitude differs minimally. Conversely, the normalized roll displays a significantly larger discrepancy between the mesh resolutions. However, the actual mean roll is very small, which means that even though the differences in normalized mean roll are large, the differences in actual mean roll are small.

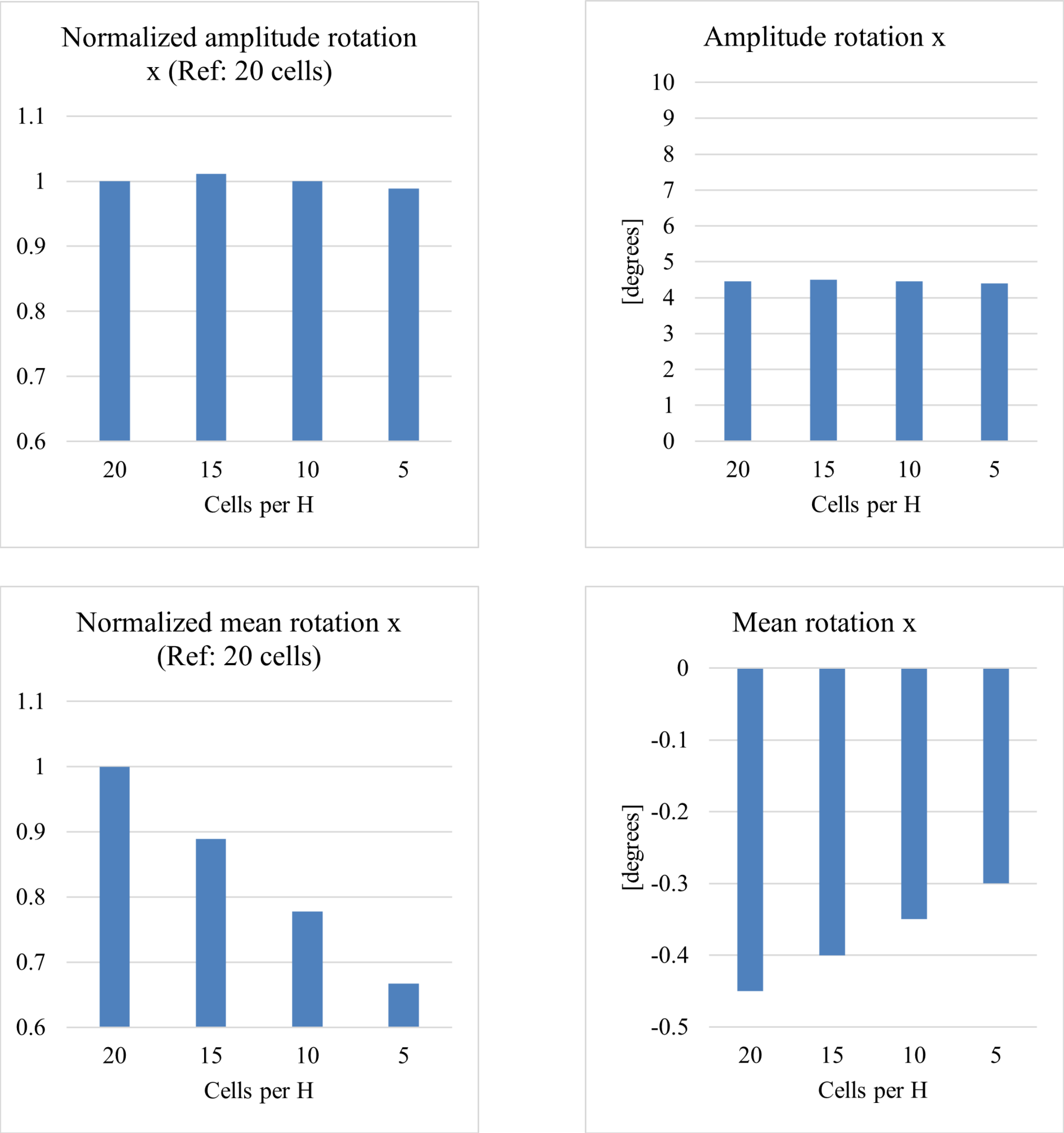

Figure 4.16: Comparison of normalized and actual roll amplitudes and mean roll (rotation around the x-axis) of the floater for the spatial study.

The resulting wave heights of the spatial discretization study are displayed in Figure 4.17. The wave height waves for the mesh resolutions all differ less than 1.5% from the reference case, indicating that the wave height is insignificantly impacted by the number of cells per wave height.

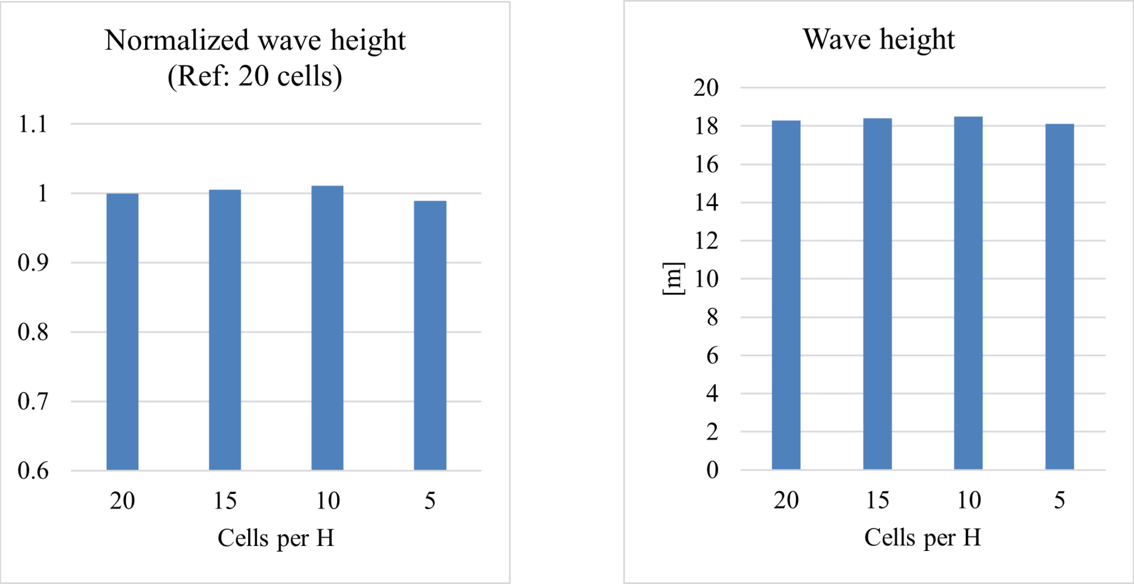

Figure 4.17: Comparison of normalized and actual wave heights for the spatial study.

The results of the spatial discretization study show that the mesh with five cells per wave height within refinement zone 1 captured the amplitudes fo the floater's position in y-direction, z-direction, rotation around the x-axis, as well as the wave height, with less than 3% discrepancy compared to the base mesh consisting of 20 cells per wave height. Based on the computational times presented in Figure 4.18, this entails a reduction of the computational time by more than 90%, if the main focus is to capture the amplitudes. Furthermore, the results suggest that the mean value of the floater's position in the y-direction and the rotation around the x-axis requires a mesh of at least 15 cells per wave height to obtain deviations of roughly 10% or less. However, it can be argued that correctly capturing the amplitudes is more important since the mean values are impacted by the simplified mooring system and therefore not really comparable to the model tests.

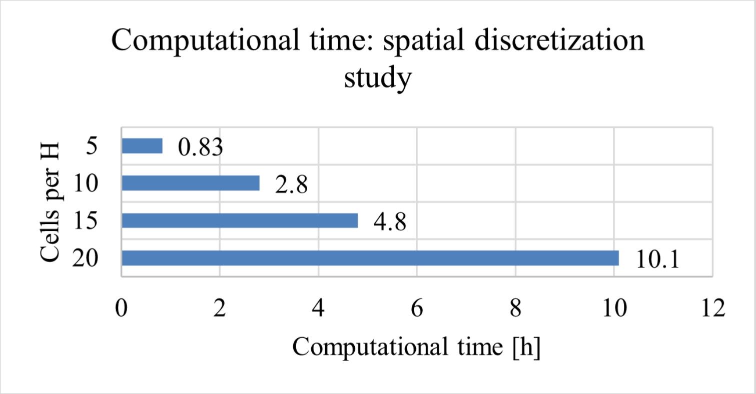

Figure 4.18: Computational times for spatial discretization study using two compute nodes (128 cores).

The results of the temporal discretization study are presented in Figures 4.19-4.22. Furthermore, the computational time of each of the simulations in the temporal discretization is detailed in Figure 4.23.

The results of the temporal discretization study, regarding the position of the floater's center of gravity in the y-direction, are displayed in Figure 4.19. It is clear from the results that both the amplitudes and the mean values of the floater's position in the y-direction vary minimally between the different temporal resolutions.

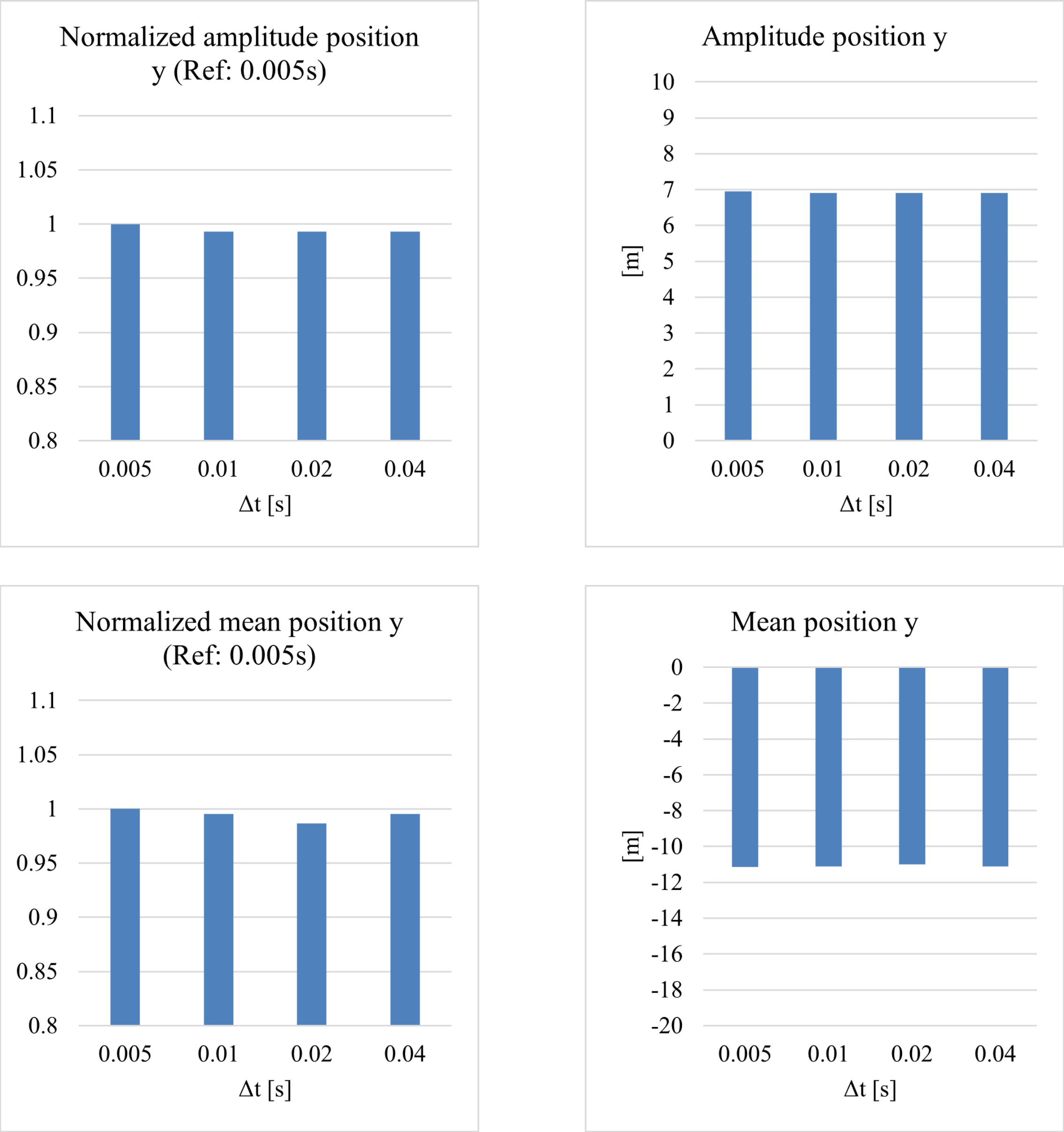

Figure 4.19: Comparison of normalized and actual amplitudes and mean positions of the floater's center of gravity in the y-direction for the temporal study.

Figure 4.20 presents the results considering the position of the floater's center of gravity in the z-direction. Both the amplitude and the mean value of the position remain consistent across all temporal discretizations. This suggests that a time step size of 0.04 seconds is sufficient to accurately capture the floater's motion in the z-direction.

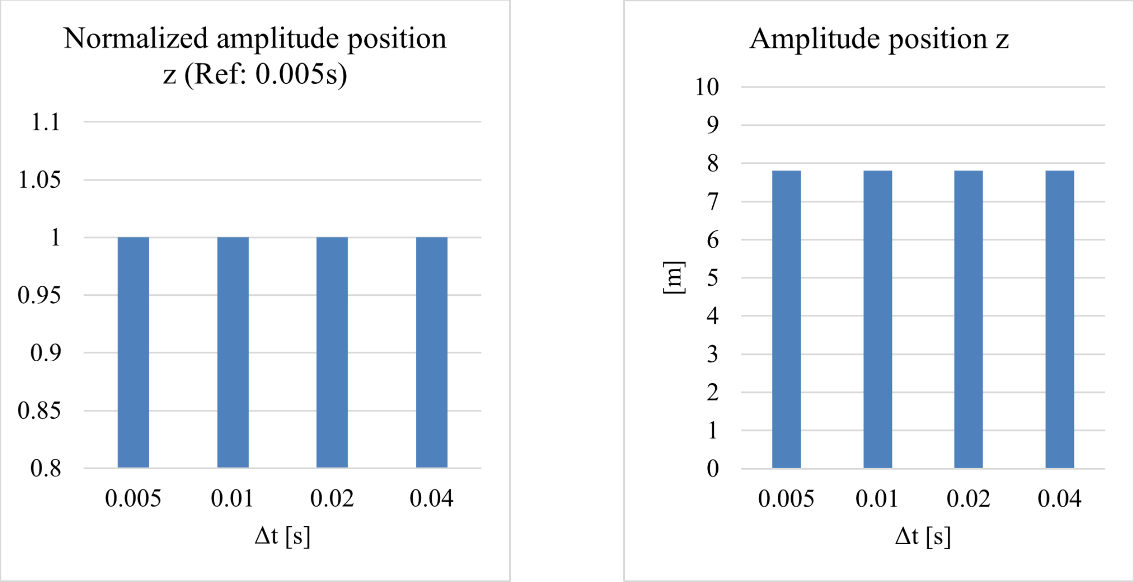

Figure 4.20: Comparison of normalized and actual amplitudes and mean positions of the floater's center of gravity in the z-direction for the temporal study.

The resulting rotation around the x-axis of the floater in the temporal discretization study is visualized in Figure 4.21. The amplitudes exhibit a deviation of less than 1.5% between the temporal discretizations. In contrast, for the mean value of the roll, the two largest time steps, 0.02 and 0.04 seconds, clearly deviate from the finer temporal discretizations. This indicates that a time step of at least 0.01 seconds is required to capture the roll of the floater.

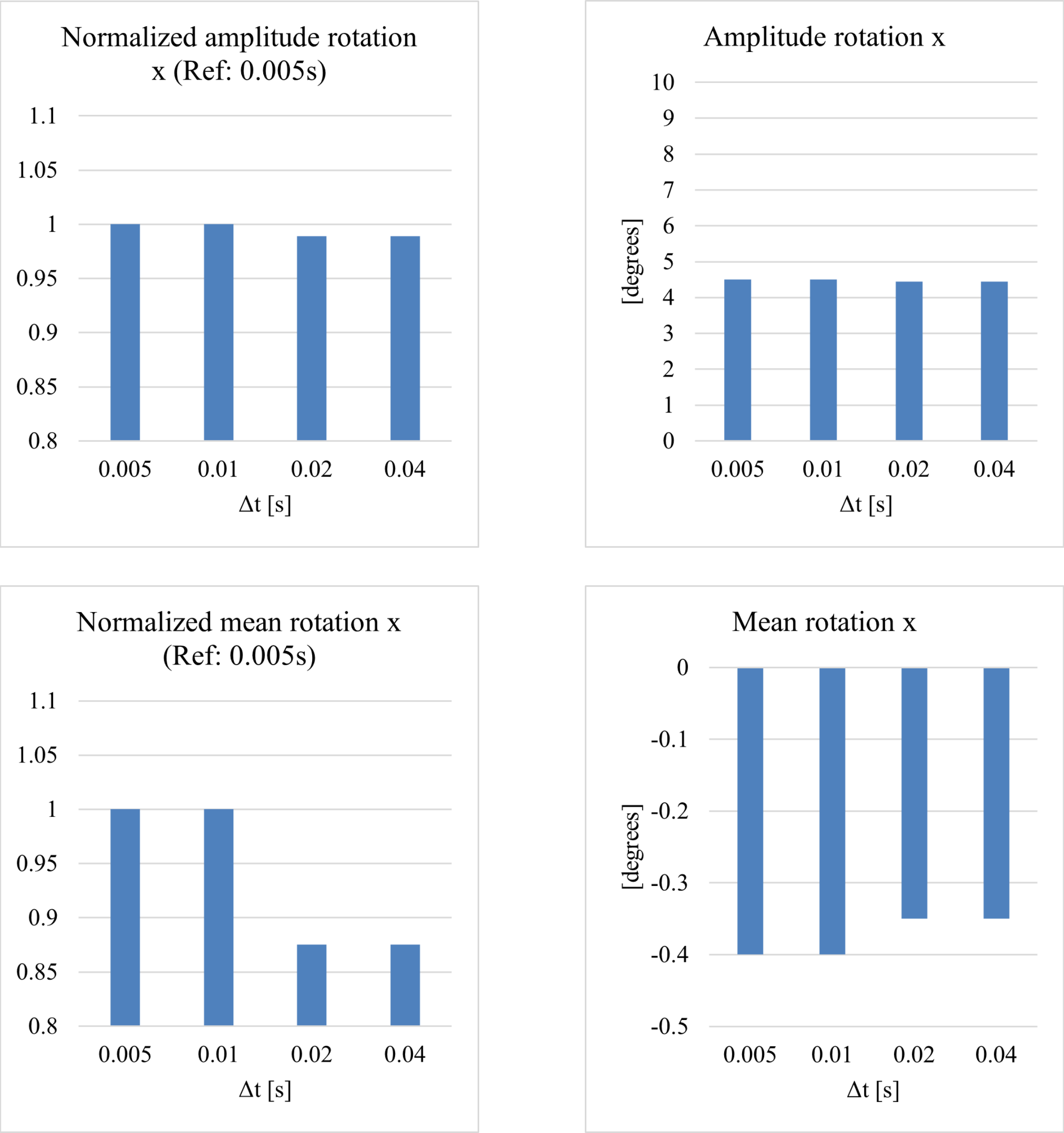

Figure 4.21: Comparison of normalized and actual amplitudes and mean values of the floater's rotation around the x-axis for the temporal study.

The resulting wave heights of the different temporal resolutions are presented in Figure 4.22. The only temporal resolution for which the wave height differs from the reference simulation is the $\Delta t = 0.04$ s. The difference in wave height between the $\Delta t = 0.04$ s simulation and the other time steps is almost 0.5 m. If the simulation had been run for a longer duration, the wave height might have differed even more, resulting in larger discrepancies regarding the floater's motion. Therefore, it can be argued that a time step of $\Delta t = 0.04$ s is insufficient to accurately capture the wave height for this specific mesh resolution.

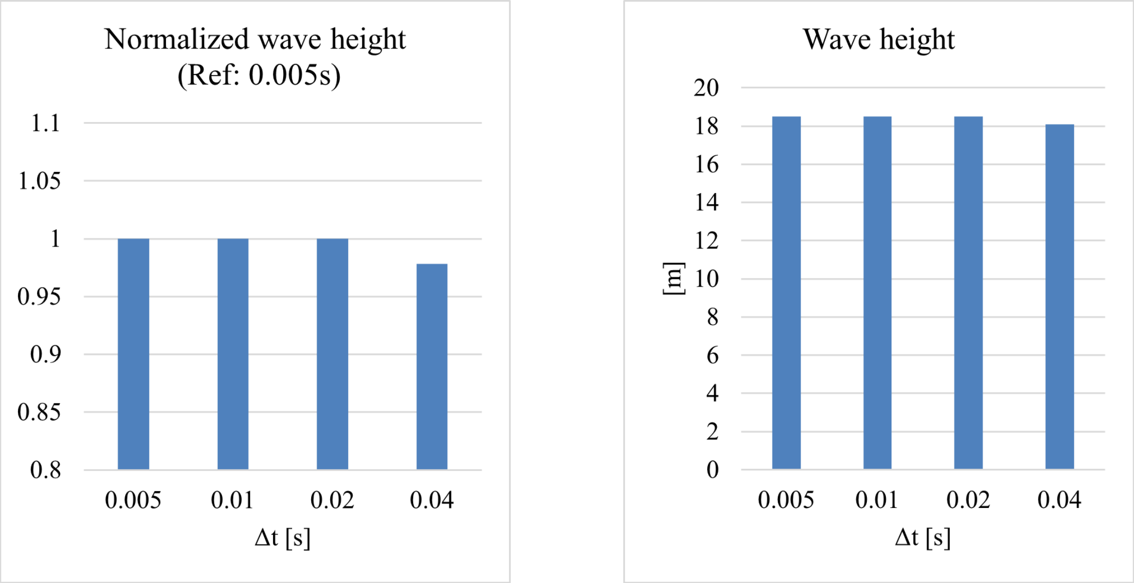

Figure 4.22: Comparison of normalized and actual wave heights for the temporal study.

The results of the temporal discretization study suggest that, for the used mesh, a time step of $\Delta t = 0.04$ s is insufficient while $\Delta t = 0.02$ can capture the amplitudes for the floater's position in y-direction, z-direction, rotation around the x-axis, as well as the wave height sufficiently. Using a time step of $\Delta t = 0.04$ s reduces the number of time steps per wave period to approximately 347.5, which still provides moderate temporal resolution. Since an implicit time integration scheme is employed, larger CFL numbers are acceptable without compromising numerical stability. However, even implicit solvers can suffer from accuracy degradation at high CFL numbers. The increased CFL number may lead to greater numerical dissipation, which could explain the observed reduction in wave height.

Additionally, $\Delta t = 0.02$ appears to adequately capture the mean position in the y-direction with small discrepancy from the finest temporal discretization. However, a smaller time step might be required to properly capture the mean value of the rotation around the x-axis. Based on the computational times presented in Figure 4.23, using a time step of $\Delta t = 0.02$ s, compared to using the smallest temporal discretization, reduces the computational time by 77.6 %, corresponding to 9.7 hours. Hence, it can be argued that $\Delta t = 0.02$ s provides a good balance between computational efficiency and solution accuracy for the used mesh.

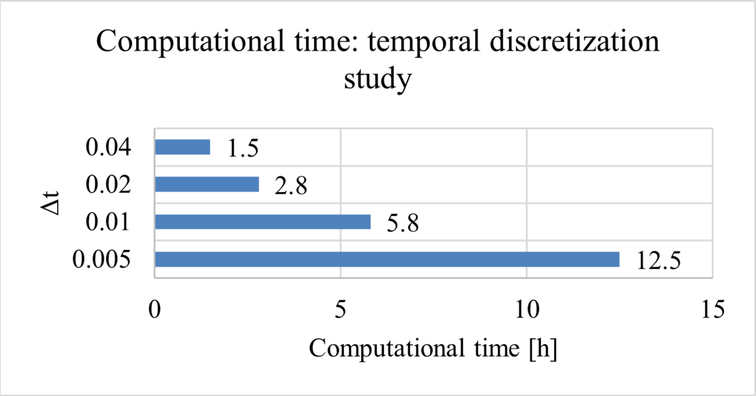

Figure 4.23: Computational times for temporal discretization study using two compute nodes (128 cores).

4.2.2.3 Comparison with Model Test

From the results in section 4.2.2.2, it can be concluded that it is possible to capture most of the compared values with acceptable accuracy, by simulating with 10 cells per wave height within mesh refinement zone 1 and a time step of $\Delta t = 0.02$ seconds. Therefore, the simulation results of this simulation are chosen for comparison with the model test data. This comparison is presented in Figures 4.24-4.27.

According to the comparison in Figure 4.24, the discrepancy is very small between the results of the simulation and the model test regarding the amplitude of the floater motion in the y-direction. Furthermore, the mean position in the y-direction differs by less than 2 meters. This difference is surprisingly small considering that a simplified mooring system was used in the simulation. Moreover, a significant discrepancy in the floater's position in y-direction could have been expected, given the finding in Section 4.1 that accurately capturing the mean water flow in the wave domain was challenging.

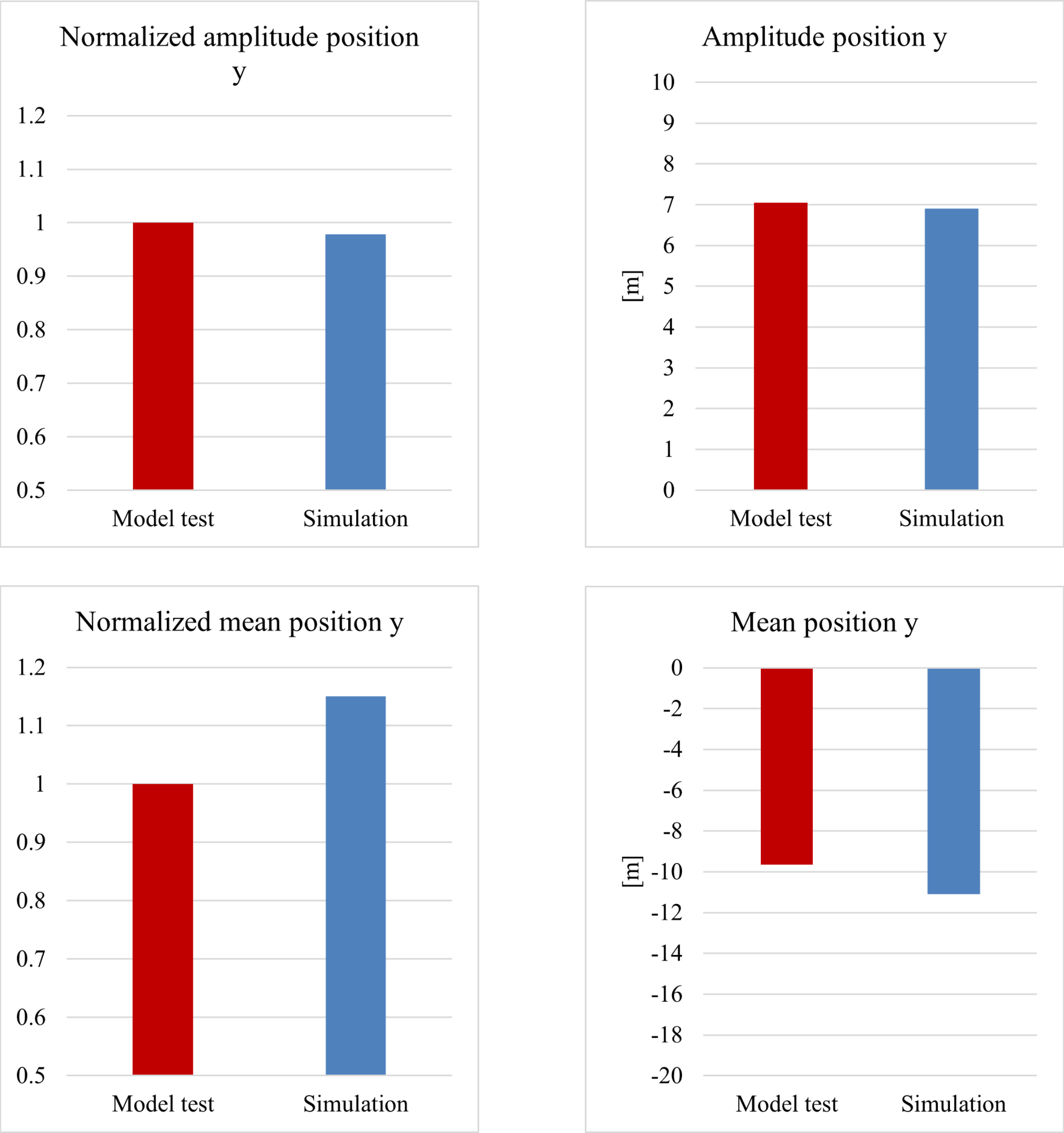

Figure 4.24: Comparison of normalized and actual amplitudes and mean values of the floater's position in y-direction in the model test and the simulation.

Figure 4.25, which presents the comparison of the amplitude of the floater's motion in the z-direction, shows that the difference is roughly 11.5 % between the simulation and the model test. Similarly to the floater's position in y-direction, the discrepancies of the position in z-direction could be due to the simplified mooring system.

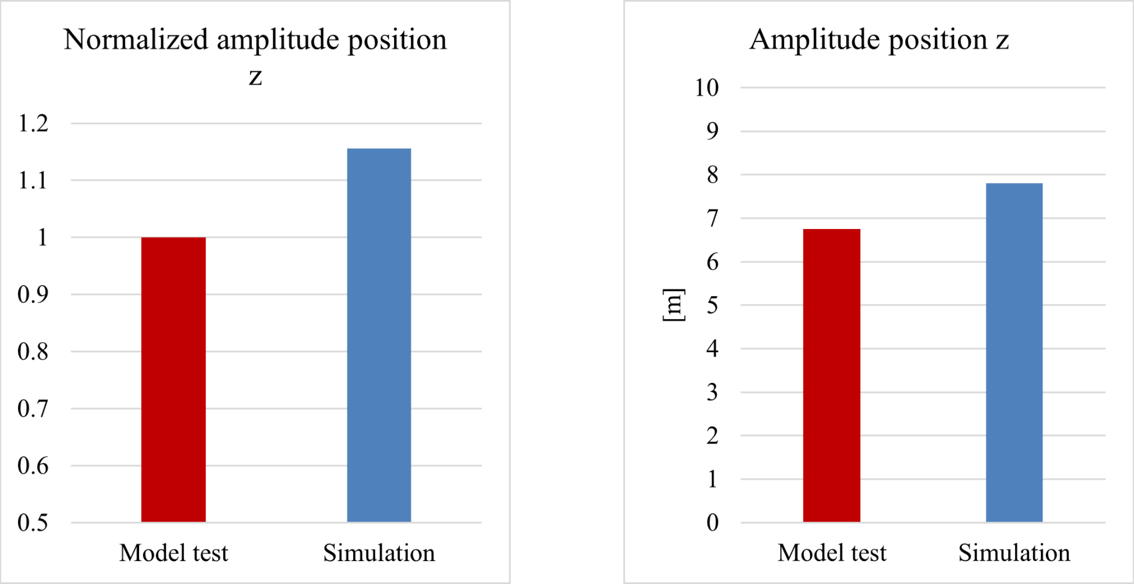

Figure 4.25: Comparison of normalized and actual amplitudes of the floater's position in z-direction in the model test and the simulation.

From Figure 4.26 it is evident that the amplitude of the floater's rotation in the x-direction differs by less than 10 %, corresponding to less than 1 degree. In contrast, the mean rotation around the x-axis has a discrepancy of almost 80 %. However, this corresponds to a difference of only about 1 degree. This suggests that the floater in the simulation has an average rotation close to level with the water, while the floater in the model test is slightly tilted in the negative y-direction.

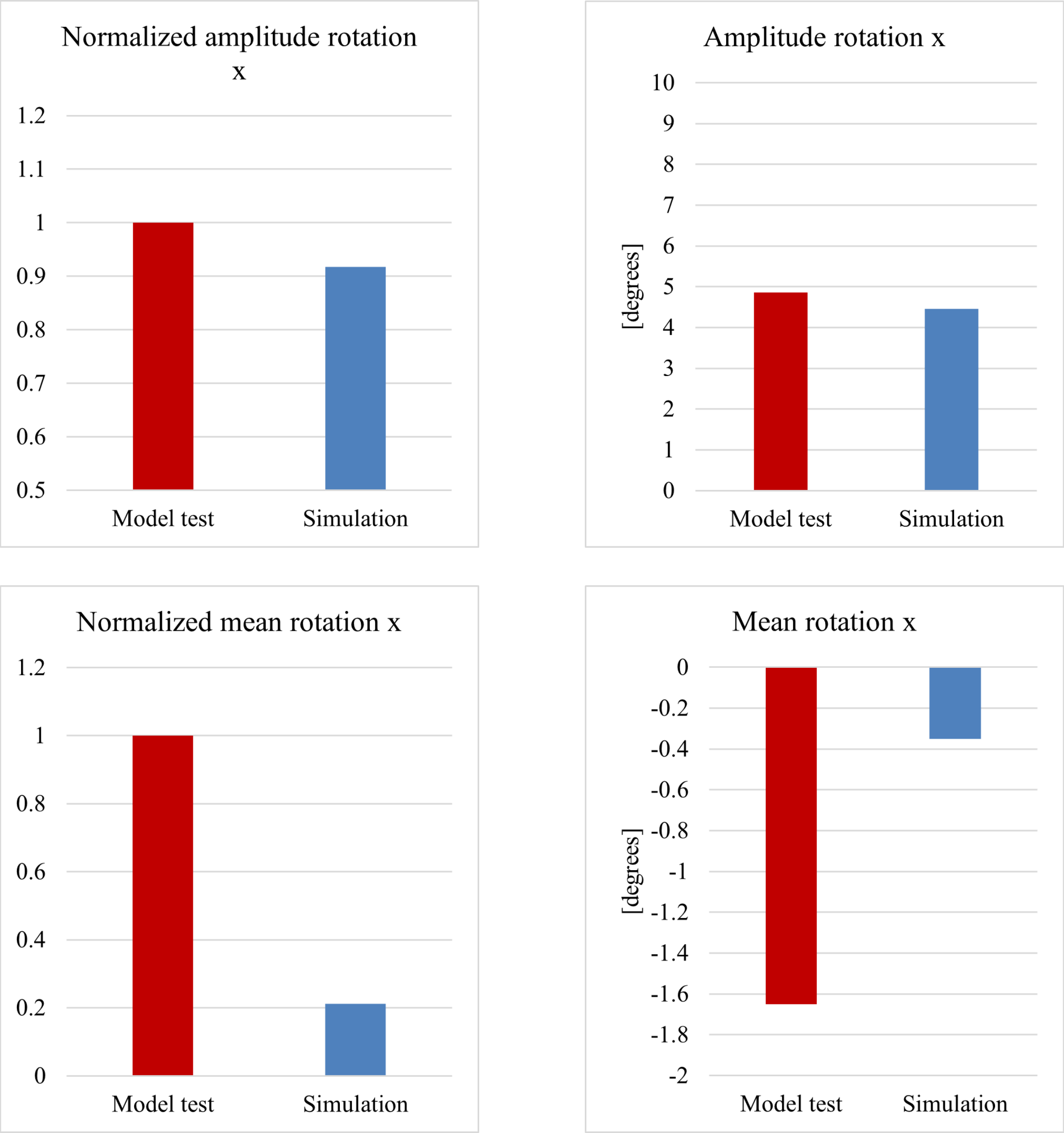

Figure 4.26: Comparison of normalized and actual amplitudes and mean values of the floater's rotation around the x-axis in the model test and the simulation.

Figure 4.27, presenting the wave height comparison, reveals that the discrepancy is approximately 5 %, equivalent to 1 meter. Although 5 % could be considered relatively small in percentage terms, a 1 meter increase in wave height could impact the floater's motion significantly. For instance, this relatively large difference in wave height could likely account for the discrepancy observed for the floater's position in the z-direction.

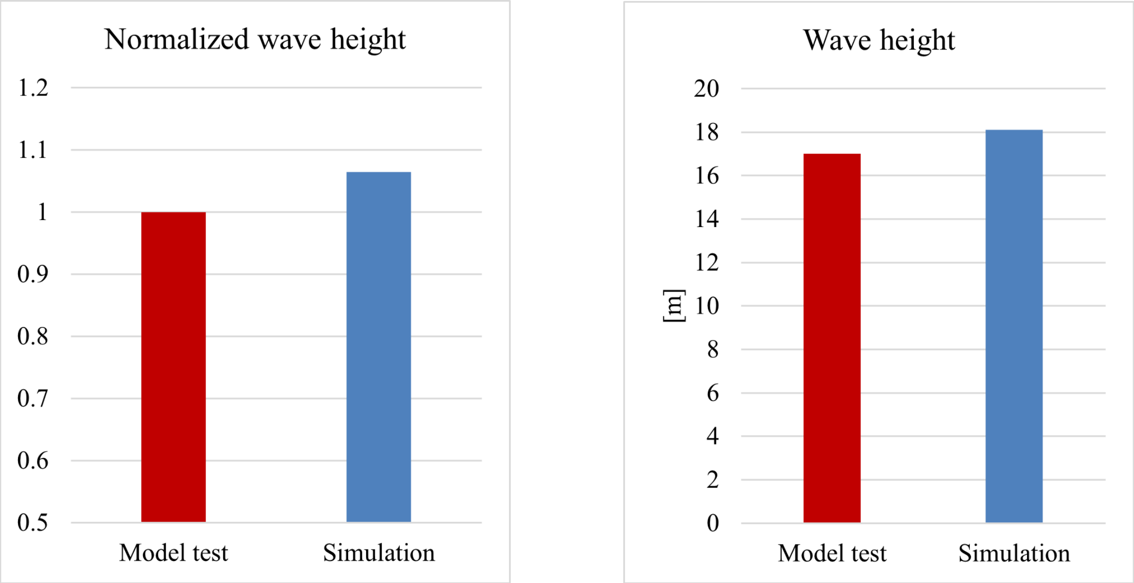

Figure 4.27: Comparison of normalized and actual wave height in the model test and the simulation.

In general, it can be concluded from the comparison that the simulation results are relatively close to the model test data. Especially considering that deviations in mean values were expected due to the simplified mooring system.

5

Conclusion

A CFD model of the semi-submersible floating platform YFloatTM was developed using fifth-order Stokes VOF waves, aiming to balance computational efficiency with solution accuracy. Two different Cases were performed as part of the development of the model.

In Case 1, simulations were performed on a smaller scale without the floater to gain a general understanding about wave simulation in CFD, by evaluating the mesh resolution required to capture wave-induced current and wave height. From the results, it can be concluded that accurately resolving wave-induced currents requires significantly finer mesh resolution than what is necessary for capturing wave height alone.

The results of Case 2 suggested that the best balance between computational efficiency and solution accuracy was achieved using 10 cells per wave height within the wave mesh refinement zone, and a time step of $\Delta t = 0.02$ s. This configuration also showed strong agreement with the model test data. In terms of efficiency, this configuration resulted in a 72 % reduction in computational time (saving 7.3 hours) compared to the finest spatial resolution, and a 77.6 % reduction (saving 9.7 hours) compared to the finest temporal resolution. In conclusion, the CFD model was shown to accurately capture the floater's dynamic response and wave interaction, with significant gains in computational efficiency achievable through optimized discretization without loss of accuracy.

5.1 Recommendations for Future Work

The following recommendations have been identified for future work:

- **Evaluate the model under a broader range of regular wave conditions:** Evaluating the model's performance under various regular wave conditions would help assess the sensitivity of the floater's response to a spectrum of sea states and validate the robustness of the model. These conditions should include variations in wave height, period, and direction.
- **Apply irregular waves to asses realistic sea states:** To further optimize the model, irregular wave conditions should be applied to mimic real realistic sea states. This is essential to capture the true behavior of the floater.

Consequently, the best spatial and temporal discretizations, in terms of computational efficiency and solution accuracy, for such simulations should also be investigated.

- **Incorporate a more realistic mooring system to increase the accuracy:** As mentioned multiple times throughout the report, the simplified mooring system may have influenced the results. Therefore, implementing a more realistic mooring system would provide more accurate floater dynamics.
- **Investigate alternative approaches to improve the computational efficiency of the model:** Investigating techniques such as scaling down the simulations or leveraging from symmetrical geometry could potentially improve computational efficiency additionally.

Bibliography

[1] International Renewable Energy Agency. *World Energy Transitions Outlook 2024: 1.5°C pathway.* 2024. URL: `www.irena.org`.

[2] Bengt Andersson et al. *Computational Fluid Dynamics for Engineers.* Cambridge University Press, 2011.

[3] Srikanth Bashetty and Selahattin Ozcelik. "Review on Dynamics of Offshore Floating Wind Turbine Platforms". In: *Energies* 14.19 (2021). ISSN: 1996-1073. DOI: `10.3390/en14196026`. URL: `https://www.mdpi.com/1996-1073/14/19/6026`.

[4] M.A. Benitz, M.A. Lackner, and D.P. Schmidt. "Hydrodynamics of offshore structures with specific focus on wind energy applications". In: *Renewable and Sustainable Energy Reviews* 44 (2015), pp. 692–716. ISSN: 1364-0321. DOI: `https://doi.org/10.1016/j.rser.2015.01.021`. URL: `https://www.sciencedirect.com/science/article/pii/S1364032115000313`.

[5] Jiri Blazek. "Chapter 7 - Turbulence Modeling". In: *Computational Fluid Dynamics: Principles and Applications (Third Edition).* Ed. by Jiri Blazek. Third Edition. Oxford: Butterworth-Heinemann, 2015, pp. 213–252. ISBN: 978-0-08-099995-1. DOI: `https://doi.org/10.1016/B978-0-08-099995-1.00007-5`. URL: `https://www.sciencedirect.com/science/article/pii/B9780080999951000075`.

[6] Chaohe Chen, Yuan Ma, and Tianhui Fan. "Review of model experimental methods focusing on aerodynamic simulation of floating offshore wind turbines". In: *Renewable and Sustainable Energy Reviews* 157 (2022), p. 112036. ISSN: 1364-0321. DOI: `https://doi.org/10.1016/j.rser.2021.112036`. URL: `https://www.sciencedirect.com/science/article/pii/S1364032121012983`.

[7] S. Gueydon, I. Bayati, and E.J. de Ridder. "Discussion of solutions for basin model tests of FOWTs in combined waves and wind". In: *Ocean Engineering* 209 (2020), p. 107288. ISSN: 0029-8018. DOI: `https://doi.org/10.1016/j.oceaneng.2020.107288`. URL: `https://www.sciencedirect.com/science/article/pii/S0029801820303322`.

[8] Rizwan Haider et al. "Review of Computational Fluid Dynamics in the Design of Floating Offshore Wind Turbines". In: *Energies* 17.17 (2024), p. 4269. DOI: `10.3390/en17174269`. URL: `https://www.mdpi.com/1996-1073/17/17/4269`.

[9] V. Heller. "8.04 - Development of Wave Devices from Initial Conception to Commercial Demonstration". In: *Comprehensive Renewable Energy.* Ed. by Ali Sayigh. Oxford: Elsevier, 2012, pp. 79–110. ISBN: 978-0-08-087873-7. DOI:

https://doi.org/10.1016/B978-0-08-087872-0.00804-0. URL: https://www.sciencedirect.com/science/article/pii/B9780080878720008040.

[10] International Renewable Energy Agency (IRENA). *Floating Offshore Wind Outlook*. IRENA, 2023. URL: https://www.irena.org/publications/2023/Jan/Floating-Offshore-Wind-Outlook.

[11] Takeo Kajishima and Kunihiko Taira. *Computational Fluid Dynamics*. Springer International Publishing, 2017. ISBN: 978-3-319-45302-6. DOI: 10.1007/978-3-319-45304-0. URL: http://link.springer.com/10.1007/978-3-319-45304-0.

[12] Georgi Kalitzin et al. "Near-wall behavior of RANS turbulence models and implications for wall functions". In: *Journal of Computational Physics* 204.1 (2005), pp. 265–291. ISSN: 0021-9991. DOI: https://doi.org/10.1016/j.jcp.2004.10.018. URL: https://www.sciencedirect.com/science/article/pii/S0021999104004164.

[13] Antonio Medina-Manuel et al. "Hydrodynamic coefficients from forced and decay heave motion tests of a scaled model of a column of a floating wind turbine equipped with a heave plate". In: *Ocean Engineering* 252 (2022), p. 110985. ISSN: 0029-8018. DOI: https://doi.org/10.1016/j.oceaneng.2022.110985. URL: https://www.sciencedirect.com/science/article/pii/S0029801822004115.

[14] Efstathios E. Michaelides, Martin Sommerfeld, and Berend van Wachen. *Multiphase Flows with Droplets and Particles, Third Edition (3rd ed.)* CRC Press, 2022. ISBN: 9781003089278. DOI: https://doi.org/10.1201/9781003089278.

[15] NASA Langley Research Center. *Wilcox k-ω Turbulence Model*. Accessed: 2025-04-24. 2025. URL: https://turbmodels.larc.nasa.gov/wilcox.html.

[16] Aldert Otter et al. "A review of modelling techniques for floating offshore wind turbines". In: *Wind Energy* 25.5 (2022), pp. 831–857. ISSN: 1099-1824. DOI: 10.1002/we.2701.

[17] A. N. Robertson et al. "OC6 phase I: Investigating the underprediction of low-frequency hydrodynamic loads and responses of a floating wind turbine". In: *Journal of Physics: Conference Series* 1618.3 (Sept. 2020), p. 032033. DOI: 10.1088/1742-6596/1618/3/032033.

[18] Siemens Digital Industries Software. *STAR-CCM+ User Guide 2410*. Accessed: 2025-04-16. 2024. URL: https://docs.sw.siemens.com/en-US/doc/226870983/PL20241127715776608.starccmp_userguide_html?audience=external.

[19] Aker Solutions. *Y-Float Generic*. Accessed: 2025-04-24. 2025. URL: https://www.akersolutions.com/what-we-do/renewable-energy-solutions/offshore-wind-solutions/floating-wind-substructures/y-float-generic/.

[20] Lu Wang et al. "Uncertainty Assessment of CFD Investigation of the Nonlinear Difference-Frequency Wave Loads on a Semisubmersible FOWT Platform". In: *Sustainability* 13.1 (2021). Published: 23 December 2020, p. 64. DOI: 10.3390/su13010064.

[21] Somaya Younoussi and Abdeslem Ettaouil. "Calibration method of the k-ω SST turbulence model for wind turbine performance prediction near stall

condition”. In: *Heliyon* 10.1 (2024), e24048. ISSN: 2405-8440. DOI: `https://doi.org/10.1016/j.heliyon.2024.e24048`. URL: `https://www.sciencedirect.com/science/article/pii/S2405844024000793`.

[22] Wenzhe Zhang et al. “Computational Fluid Dynamics (CFD) applications in Floating Offshore Wind Turbine (FOWT) dynamics: A review”. In: *Applied Ocean Research* 150 (2024), p. 104075. ISSN: 0141-1187. DOI: `https://doi.org/10.1016/j.apor.2024.104075`. URL: `https://www.sciencedirect.com/science/article/pii/S0141118724001974`.

[23] Y. Zhang and B. Kim. “A Fully Coupled Computational Fluid Dynamics Method for Analysis of Semi-Submersible Floating Offshore Wind Turbines Under Wind-Wave Excitation Conditions Based on OC5 Data”. In: *Applied Sciences* 8.11 (2018), p. 2314. DOI: `10.3390/app8112314`. URL: `https://doi.org/10.3390/app8112314`.

A

Appendix: Case 1

Figure A.1 presents the mean water velocity in x-direction, over the last five wave periods, at different water depths for the simulation z=0.0024 x=2z base=4z. At the depths for which the mean velocity was positive, the mean velocity was multiplied by the vertical distance to the point probe below (0.02 m) and the resulting values were summed to determine the total mean water flow in positive x-direction. The calculation of the total mean water flow is detailed in Table A.1.

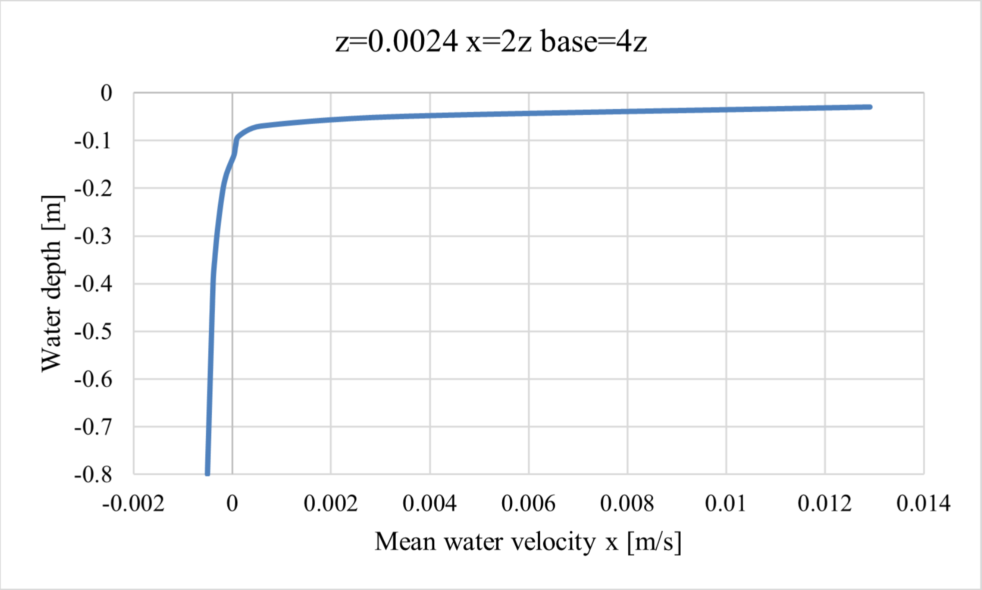

Figure A.1: Mean water velocities in x-direction at different depths for the simulation z=0.0024 x=2z base=4z.

Table A.1: Calculated positive mean volume flow rates per meter in x-direction over the final five wave periods. The positive mean water velocities (V_x) at each point probe were multiplied by the vertical distance to the probe below (0.02 m), and the resulting values were summed to determine the total volume flow rate per meter.

Water depth [m]	Mean V$_x$ [m/s]	V_x×0.02 [(m^3/s)/m]
-0.03	0.012904049	0.000258081
-0.05	0.003345847	6.69169E-05
-0.07	0.000574573	1.14915E-05
-0.09	0.000142149	2.84299E-06
-0.11	6.92492E-05	1.38498E-06
-0.13	3.6024E-05	7.20479E-07
	Sum=	**0.000341438**

For each simulation in Case 1, the resulting total mean water flow in positive x-direction and the resulting wave height are summarized in Table A.2.

Table A.2: Resulting Mean volume flows and wave heights for the mesh study performed for case 1.

Grid	Mean volume flow [(m^3/s)/m]	H / $H_{\text{specified}}$
Base mesh comparison		
z=0.003 x=4z base=16z	0.0003721	1.006
z=0.003 x=4z base=8z	0.0002341	1.002
z=0.003 x=4z base=4z	0.0002022	1.005
x cell size comparison		
z=0.003 x=8z base=16z	0.0012035	0.9687
z=0.003 x=4z base=8z	0.0002341	1.002
z=0.003 x=2z base=4z	0.0001976	1.006
z cell size comparison		
z=0.012 x=2z base=4z	0.0007796	0.9590
z=0.006 x=2z base=4z	0.0002028	0.9932
z=0.004 x=2z base=4z	0.0001543	0.9984
z=0.003 x=2z base=4z	0.0001976	1.006
z=0.0024 x=2z base=4z	0.0003414	1.000
z=0.002 x=2z base=4z	0.0003910	0.9928

DEPARTMENT OF MECHANICS AND MARITIME SCIENCES
CHALMERS UNIVERSITY OF TECHNOLOGY
Gothenburg, Sweden
www.chalmers.se

CHALMERS
UNIVERSITY OF TECHNOLOGY